Proton temperature anisotropies in the plasma environment of Venus

A. Bader[1,2,3], G. Stenberg Wieser[1], M. André[4], M. Wieser[1], Y. Futaana[1], M. Persson[1,5], H. Nilsson[1], T. L. Zhang[6]

[1]Swedish Institute of Space Physics, Kiruna, Sweden
[2]Luleå tekniska universitet, Kiruna, Sweden
[3]now: Department of Physics, Lancaster University, Lancaster, UK
[4]Swedish Institute of Space Physics, Uppsala, Sweden
[5]Umeå universitet, Umeå, Sweden
[6]Space Research Institute, Austrian Academy of Science, Graz, Austria

Key Points:

- We present maps of the perpendicular and parallel proton temperatures and their ratio in the plasma environment around Venus
- The largest perpendicular temperature anisotropy with a median temperature ratio of about 3/2 is found in the near subsolar magnetosheath
- The region with the largest observed temperature anisotropy coincides with observations of proton cyclotron and mirror mode waves

This article has been accepted for publication and undergone full peer review but has not been through the copyediting, typesetting, pagination and proofreading process which may lead to differences between this version and the Version of Record. Please cite this article as doi: 10.1029/2019JA026619

Corresponding author: A. Bader, a.bader@lancaster.ac.uk

Abstract

Velocity distribution functions (VDFs) are a key to understanding the interplay between particles and waves in a plasma. Any deviation from an isotropic Maxwellian distribution may be unstable and result in wave generation. Using data from the ion mass spectrometer IMA (Ion Mass Analyzer) and the magnetometer MAG onboard Venus Express, we study proton distributions in the plasma environment of Venus. We focus on the temperature anisotropy, that is, the ratio between the proton temperature perpendicular ($T_\perp$) and parallel ($T_\parallel$) to the background magnetic field. We calculate average values of $T_\perp$ and $T_\parallel$ for different spatial areas around Venus. In addition we present spatial maps of the average of the two temperatures and of their average ratio. Our results show that the proton distributions in the solar wind are quite isotropic, while at the bow shock stronger perpendicular than parallel heating makes the downstream VDFs slightly anisotropic ($T_\perp/T_\parallel > 1$) and possibly unstable to generation of proton cyclotron waves or mirror mode waves. Both wave modes have previously been observed in Venus' magnetosheath. The perpendicular heating is strongest in the near subsolar magnetosheath ($T_\perp/T_\parallel \approx 3/2$), which is also where mirror mode waves are most frequently observed. We believe that the mirror mode waves observed here are indeed generated by the anisotropy. In the magnetotail we observe planetary protons with largely isotropic VDFs, originating from Venus' ionosphere.

1 Introduction

Venus is the second planet from the Sun, and Earth's closest neighbor in the solar system. While its size and internal structure are very similar to those of the Earth, it lacks an intrinsic magnetic field. The solar wind can therefore directly interact with Venus' atmosphere [e.g., *Futaana et al.*, 2017]. As the solar wind meets the planet, the frozen-in magnetic field carried by the charged solar wind particles causes electrical currents in the ionosphere and a so-called induced magnetosphere is formed. The solar wind is diverted around the planet and the interplanetary magnetic field (IMF) drapes around the obstacle [e.g., *Luhmann*, 1986]. While an elongated magnetotail is observed on the nightside of Venus, the magnetic field piles up and creates a magnetic barrier on the dayside [e.g., *Zhang et al.*, 1991]. This barrier shields the planet's atmosphere from the solar wind [e.g., *Stenberg Wieser et al.*, 2015] and causes the formation of an upstream bow shock where the solar wind particles are slowed down to subsonic speeds. The so-called induced magnetosphere boundary (IMB) separates regions dominated by solar wind ions and ionospheric ions, respectively [e.g., *Zhang et al.*, 2008a].

The manifold of interactions between the solar wind and Venus' induced magnetosphere have been investigated by several missions since the early 1960s. After several successful flyby missions, Venera-9 and -10 were the first spacecraft to orbit and land on Venus. The exploration of the Venus plasma environment continued with NASA's Pioneer Venus Orbiter (PVO) [*Colin*, 1980], which was in orbit around the planet between 1978 and 1992. The most recent orbiter of importance for the space plasma physics community was the European Space Agency's Venus Express (VEX, in orbit 2006-2014) [*Titov et al.*, 2006; *Svedhem et al.*, 2007], which was equipped with the plasma package ASPERA-4 in order to study atmospheric outflow and the interaction mechanisms contributing to it [*Barabash et al.*, 2007] .

Throughout the years of exploration, many different plasma wave modes have been observed around Venus. Different studies have focused either on the statistical properties of the fluctuations or on individual waves modes. Early measurements of PVO near the ionopause confirmed the presence of whistler waves likely to be associated with lightning in the atmosphere of Venus [*Scarf et al.*, 1980a,b; *Russell et al.*, 2007]. Later, VEX measurements suggested mirror mode (MM) waves in the magnetosheath region [*Volwerk et al.*, 2008a,b, 2016] as well as proton cyclotron (PC) waves upstream of the bow shock [*Delva et al.*, 2008a,b, 2011]. Proton cyclotron waves associated with the pickup of freshly

ionized planetary exospheric particles had previously been observed upstream of Mars using Phobos and Mars Global Surveyor spacecraft data [e.g., *Russell et al.*, 1990; *Delva and Dubinin*, 1998; *Brain et al.*, 2002], but were not detected upstream of the bow shock in PVO data [*Russell et al.*, 2006a]. An independent attempt to identify pickup PC waves in VEX data also failed, with most of the waves observed close to the local proton cyclotron frequency appearing to be generated by backstreaming protons reflected at the parallel bow shock [*Wei et al.*, 2011].

Proton cyclotron waves are, however, certainly present in the magnetosheaths of both Mars and Venus [*Russell et al.*, 2006a]. A recent statistical study, *Fränz et al.* [2017], is one of very few studies combining particle and field measurements to investigate the plasma wave environment around Venus. They used mostly VEX electron and magnetometer data to identify and characterize different ultra low frequency (ULF) plasma waves. Their wave mode identification scheme is based on MHD theory [*Song et al.*, 1994] and they find that Alfvén-like waves are generally dominating in the solar wind and the magnetosheath, but sometimes mirror mode waves can also be dominant.

To understand both the origin of the observed waves and the role they play in Venus' induced magnetosphere it is important to carefully study associated particle distributions. For example, the ion pickup process can lead to ring-beam velocity distributions, which are unstable and considered to be one way of generating ion cyclotron waves [e.g., *Tsurutani and Smith*, 1986; *Delva et al.*, 2011]. Energy can also be transferred the opposite way: from waves to particles. Wave-particle interaction is established as one of the main ion acceleration mechanisms leading to ion escape in the Earth's polar cusp [e.g., *Norqvist et al.*, 1998; *Waara et al.*, 2011] and may also be important for acceleration of ions at Venus [e.g., *Brain et al.*, 2016].

Just like at Earth, there is a continuous escape of atmospheric ions from Venus. A review of PVO data estimated the total ion outflow from Venus to be $10^{25}\,s^{-1}$ [*Russell et al.*, 2006b], while studies using VEX data during solar minimum reported outflow rates of about $(2-6)\times10^{24}\,s^{-1}$ [e.g., *Fedorov et al.*, 2011; *Nordström et al.*, 2013; *Persson et al.*, 2018]. Ions are accelerated and removed from the induced magnetosphere through a combination of different mechanisms - for example, through tailward acceleration in the plasma sheet by the magnetic tension force [e.g., *Dubinin et al.*, 2013], through magnetotail reconnection processes [e.g., *Dubinin et al.*, 2012; *Zhang et al.*, 2012] or through pickup and acceleration by the convection electric field in the solar wind [e.g., *McEnulty et al.*, 2010]. The importance of wave-particle interaction for ion escape is yet to be investigated.

In this study we concentrate on proton velocity distribution functions (VDFs) and focus especially on temperature anisotropies. In an electron-proton plasma different proton temperatures perpendicular and parallel to the magnetic field may generate waves. If $T_\perp > T_\parallel$, the plasma may be unstable to both proton cyclotron waves and mirror mode waves [*Gary*, 1992], which are two of the wave modes identified in the environment around Venus. Observations of temperatures and temperature anisotropies in the solar wind and the magnetosheath are also of fundamental interest as they provide clues to how heating occurs at a collisionless shock and how the solar wind is generated [*Parks et al.*, 2016].

Here we use ion and magnetic field data recorded by Venus Express to perform a statistical analysis of proton VDFs in the vicinity of Venus. We compute average maps of the proton temperatures perpendicular and parallel to the ambient magnetic field as well as of the temperature anisotropy ($T_\perp/T_\parallel$). We find that the temperature ratio characterizes the different spatial regions around the planet and we compare and discuss our results in the light of previously published wave observations.

2 Instrumentation and data set

All ion data used in this paper has been obtained by the Ion Mass Analyzer (IMA), one of the sensors that are part of the ASPERA-4 instrument [*Barabash et al.*, 2007], and the magnetic field data was recorded by the magnetometer (MAG) [*Zhang et al.*, 2006] on board Venus Express. The Venus Express spacecraft was placed in a highly elliptical orbit around Venus with a periapsis altitude of about 250 km and an apoapsis altitude of about 66,000 km. Its orbit was quasi-polar with an orbital period of 24 hr.

IMA is an imaging mass spectrometer capable of resolving ion flow direction, energy per charge E/q and mass per charge m/q. Its cylindrical symmetry provides an intrinsic field of view of $4.5^\circ \times 360^\circ$ in the azimuthal plane (the aperture plane), divided into 16 azimuthal sectors of 22.5° each. An electrostatic deflector system varies the elevation angle (the angle with respect to the aperture plane) in 16 steps up to $\pm 45^\circ$ with respect to the viewing plane, resulting in a total field of view of $90^\circ \times 360^\circ$. The elevation stepping was sometimes reduced to 8 steps, covering the same range of elevation angles.

Ion energy separation occurs in a cylindrically symmetric top hat electrostatic analyzer, scanning from 12 eV/q to 30 keV/q in 96 logarithmic steps with an energy resolution of 7%. All particles exiting the electrostatic analyzer at a certain energy step have the same energy per charge, controlled by the voltage between its plates. The remaining ions are then separated according to their mass by a circular magnetic separation system. They are deflected from the symmetry axis as they pass the magnetic field region, with the magnitude of the deflection depending on the ion momentum. As a result, different ion species hit the position sensitive detector plate at different radial distances. The microchannel plate position detection system has 32 concentric radial mass rings and 16 azimuthal sectors providing mass and angular resolution.

A measurement of ion fluxes in a 2D-plane (an energy sweep) with a fixed elevation angle takes 12 s and gives the full mass and energy ranges in the instantaneous field of view; a scan over the total field of view is completed every 192 s. When converting the data to physical units, the original 32 mass ring numbers are converted to units of amu/q (atomic mass units per charge). In this study we only use data corresponding to H^+, i.e. 1 amu/q. The separation method is described in detail in *Fedorov et al.* [2011].

The magnetometer (MAG) provided the magnetic field direction and magnitude [*Zhang et al.*, 2006]. MAG measures the magnetic field vector with a resolution of at least 1 s. In this study a processed 4 s-resolution dataset is used.

We have used all available data between May 2006 and December 2009, representing nearly 4 years of continuous coverage around solar minimum. The dataset is equal to what has been used by *Nordström et al.* [2013] for the estimation of ion outflow rates.

3 Reference frames

Three different reference frames are used in this study. All observations are originally made in the reference frame fixed to the respective instrument, and each instrument reference frame can be converted to an agreed spacecraft-fixed frame. The spacecraft-fixed Y_{VEX}-direction is parallel to the symmetry axis of IMA; measurements at zero elevation are therefore taken in the X_{VEX}-Z_{VEX} plane. Positive elevation angles correspond to positive Y_{VEX} values.

In general, any measured plasma population moves with respect to the spacecraft. The temperatures we are after, however, are defined in the plasma reference frame, so in order to estimate them we have to transform the observations to a reference system moving with the plasma. The procedure for finding and transforming the observations to the plasma reference frame is described in the following section.

To place single measurements in the environment around the planet, we use the Venus Solar Orbit (VSO) frame. The VSO-frame is centered on Venus, with $+X_{\mathrm{VSO}}$ being directed from Venus' center of gravity toward the Sun. The VSO system is further defined based on the orbital plane of Venus, with Z_{VSO} pointing northward and perpendicular to the orbital plane and Y_{VSO} completing the right-hand system. The orbit of Venus therefore follows the $-Y_{\mathrm{VSO}}$ direction, with $+Y_{\mathrm{VSO}}$ pointing toward the dawn side.

4 Data analysis method

Our goal is to estimate the proton temperatures in the space environment around Venus and to study any temperature anisotropies. In the following sections we describe how VDFs are obtained from IMA ion flux measurements, how the plasma bulk velocity is determined and how the VDFs are fitted with anisotropic Maxwellian distributions. We furthermore show how we obtain statistical maps from our results. To improve the overall numerical stability of the fitting process, bulk velocity and temperatures are fitted in two separate steps as shown in the following sections.

4.1 Obtaining VDFs from ion flux measurements

Every 192 s IMA produces a 3D flux distribution covering the $90° \times 360°$ field of view. We use mass-separated data which only contain the observed proton fluxes. The fully differential proton flux distribution $J(E, \Omega)$ is a a function of the energy E and the solid angle Ω corresponding to the current viewing direction of the instrument. This differential flux is converted to a velocity distribution function, $f(\mathbf{v})$, by integrating over the solid angle under which it has been measured. The velocity distribution function is then given by

$$f(\mathbf{v}) = \frac{m^2}{2E} J(E, \Omega), \tag{1}$$

as described in *Fränz et al.* [2007].

4.2 Determining the bulk velocity

The observed proton populations typically have a bulk motion relative to the spacecraft. The first step of our analysis is therefore to determine and subtract the bulk velocity $\mathbf{v}_{\mathrm{bulk}}$ for each observation (each 192 s long scan). A good way to determine $\mathbf{v}_{\mathrm{bulk}}$ turned out to be by fitting each VDF with a 3D isotropic Gaussian of the form

$$f(\mathbf{v}) = a \cdot \exp\left(-\frac{(\mathbf{v} - \mathbf{v}_{\mathrm{bulk}})^2}{b}\right) \tag{2}$$

where $\mathbf{v}$ is the observed velocity and a and b are scaling factors. We use a fitting algorithm here, as a more straightforward determination of the bulk velocity by integration is problematic for cases with incomplete or uneven phase space coverage.

We used the orthogonal distance regression (ODR) algorithm [*Boggs and Rogers*, 1990] for fitting in this study. This algorithm automatically compensates for problems in which the model parameters and/or unknown errors in the independent variables vary widely in magnitude and has been shown to produce better results than ordinary least squares regression at no additional performance cost. Further details are available in the documentation of the Scipy ODRPACK software package (`https://docs.scipy.org/doc/external/odrpack_guide.pdf`).

For about 8% of proton VDFs considered, no fit could be obtained due to insufficient data coverage (we require at least 100 nonzero data points to attempt a fit), the bulk plasma flow being outside the instrument's field of view, or the lack of convergence of the fitting procedure. Further 23% of the proton VDFs were considered failed by some of the goodness of fit tests described in section 4.5. The affected VDFs are evenly spread

throughout each region of interest. Note that the bulk velocity in the Venus rest frame is obtained by subtracting the spacecraft velocity from $\mathbf{v}_{\text{bulk}}$.

An example of a bulk velocity determination is shown in Figures 1 and 2a. The plots show all single measurements made during a scan, that is each energy and each direction, converted to velocity space in the spacecraft reference frame. The instrument has a limited angular resolution of 4.5°× 22.5° (see section 2), but in this figure each observation is represented by the boresight direction. Similarly, the energy is taken as the central energy of each energy bin. The fitted bulk velocity for this case is shown as a black and yellow star in Figure 2a.

Figures 1a, 2a and 2b show the same 3D distribution with two slightly different viewing angles, respectively, to better illustrate the 3D configuration. Additionally, the two panels may be viewed as a stereo image if so desired, although this is not essential for further understanding of the data presented. They are intended for parallel viewing; an illusion of depth is achieved by fusing the left hand panel (seen with the left eye) with the right hand panel (seen with the right eye). This can be done either by using simple parallel viewing glasses or a card placed edge on between the panels or, with some training, without any aid by free-viewing.

4.3 Fitting the VDFs

Translating the whole VDF by $-\mathbf{v}_{\text{bulk}}$ moves the measurement into an arbitrarily rotated bulk plasma reference frame such that all data points are associated with a velocity relative to the bulk plasma motion and not relative to the spacecraft.

Next we compute the angle between these velocities in the bulk plasma frame and the local instantaneous magnetic field direction $\mathbf{B}$ (the pitch angle α) for all data points in the distribution. $\mathbf{B}$ is hereby averaged from all magnetic field vectors obtained during the 192 s IMA scan. Practically, we achieve this by rotating the so far arbitrarily oriented bulk plasma frame such that $\mathbf{B}$ coincides with the Z-axis. Figure 2b shows the VDF from Fig. 2a after it was shifted and rotated. We then convert each data point from Cartesian coordinates in velocity space into spherical coordinates. The polar angle is then equal to the pitch angle α, the azimuthal angle lies in the X-Y-plane of Figure 2 and the radial component is the velocity difference between the data point and the bulk velocity.

Different perpendicular directions are not considered in this study; we assume symmetry around the magnetic field direction. The azimuthal angle of the data points is therefore being discarded. We are left with two coordinates for each data point: its absolute velocity relative to the bulk motion and its pitch angle. Figure 3 shows the collapsed velocity distribution obtained from the VDF in Figures 1 and 2.

We fit our collapsed velocity distribution with a 2D anisotropic Maxwellian of the form

$$f(\mathbf{v}) = \frac{n}{\pi^{3/2} v_{\text{th}\parallel} v_{\text{th}\perp}^2} \exp\left(-\frac{v_\perp^2}{v_{\text{th}\perp}^2} - \frac{v_\parallel^2}{v_{\text{th}\parallel}^2}\right) \tag{3}$$

where $v_\perp$ and $v_\parallel$ are the velocity components perpendicular and parallel to $\mathbf{B}$, n the ion number density and $v_{\text{th}\perp} = \sqrt{2k_B T_\perp/m}$ and $v_{\text{th}\parallel} = \sqrt{2k_B T_\parallel/m}$ the thermal velocities perpendicular and parallel to $\mathbf{B}$, respectively. In the expressions for the thermal velocities $T_\perp$ and $T_\parallel$ are the perpendicular and the parallel temperatures, m the proton mass and k_B the Boltzmann constant. Similar as for the bulk velocity fit in section 4.2, we use an orthogonal distance regression algorithm. Figure 3 shows the contours of the Maxwellian fit for the example VDF.

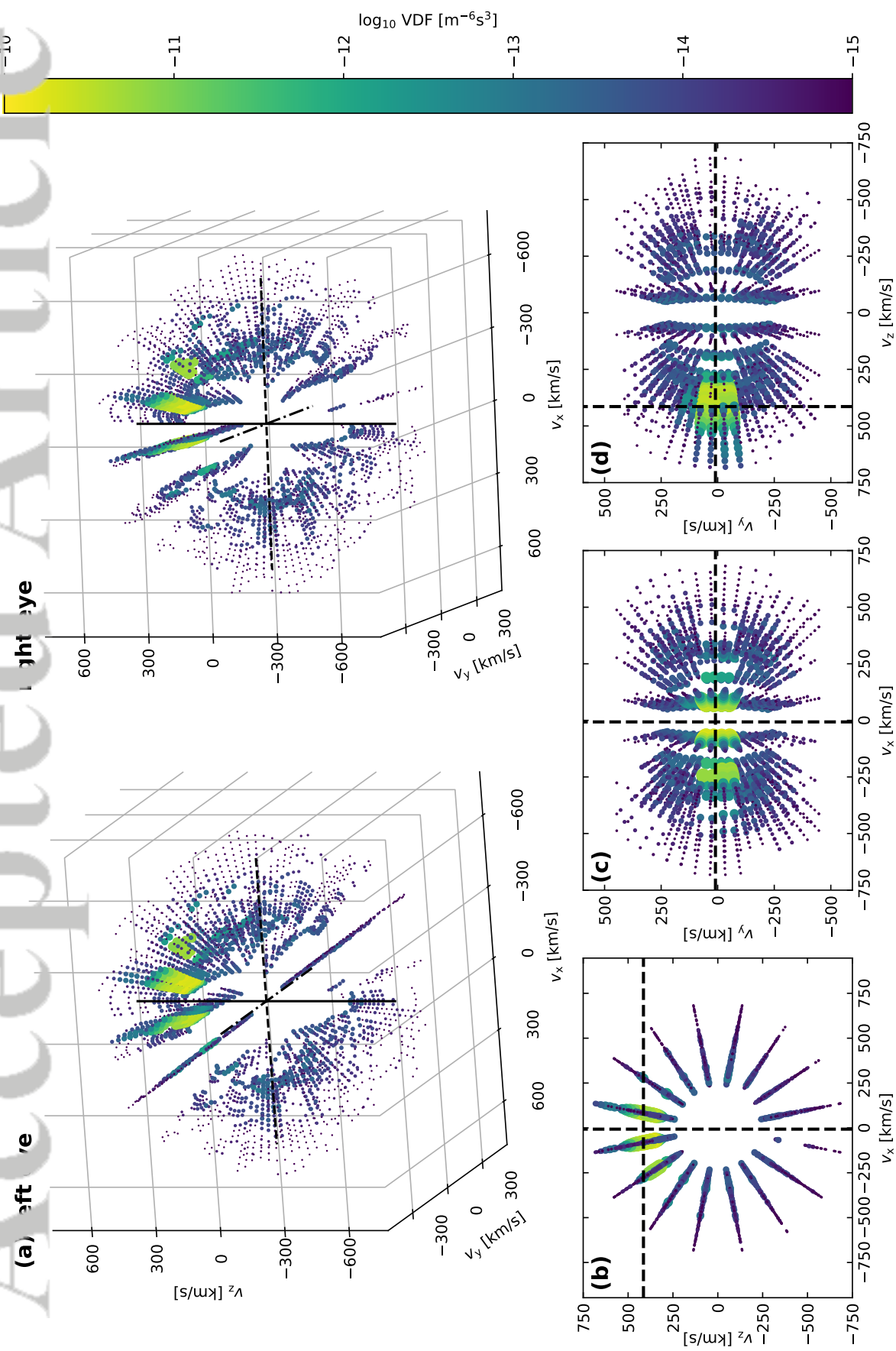

Figure 1. (a) Stereo figure of a single proton VDF measured on July 14, 2006 at approximately $X_{VSO} = -1\,R_V$, $R_{VSO} = 2.1\,R_V$ in the solar wind. The distribution is plotted in instrument-fixed VEX-coordinates. The remaining panels show projections as seen from (b) the $-Y_{VEX}$-direction, (c) the $+Z_{VEX}$-direction and (d) the $+X_{VEX}$-direction. Dashed black lines mark the bulk velocity as determined by a 3D isotropic Gaussian fit.

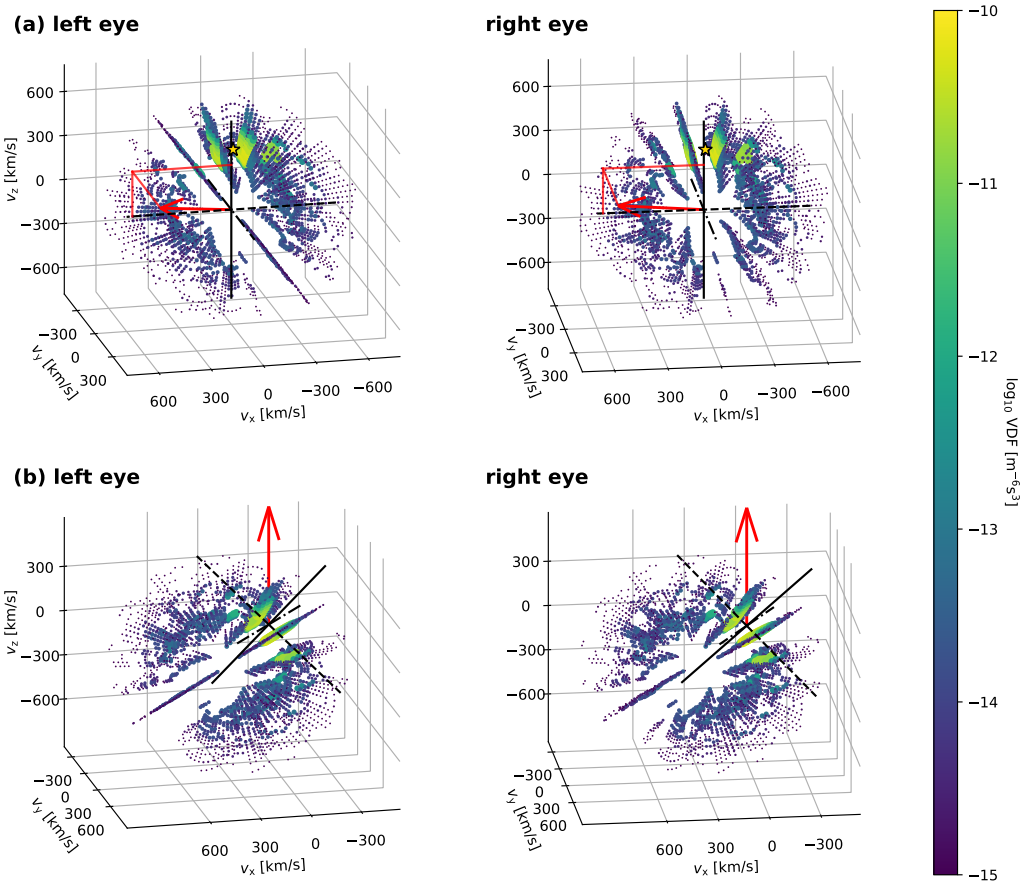

Figure 2. The same proton VDF as in Figure 1, again shown as a stereo figure. (a) The VDF as originally measured in the VEX frame, the bulk velocity is marked by a black-and-yellow star. The local magnetic field direction during the time of the measurement is indicated by a red arrow. Black dashed (X_{VEX}), dashed-dotted (Y_{VEX}) and solid (Z_{VEX}) lines along the coordinate axes and intersecting at (0,0,0) as well as some auxiliary lines help with the 3D perception. (b) The same distribution after it has been shifted such that the bulk velocity coincides with (0,0,0) and then rotated such that the magnetic field **B** points along the Z-axis. The black lines correspond to the coordinate system axes before the rotation of the shifted VDF.

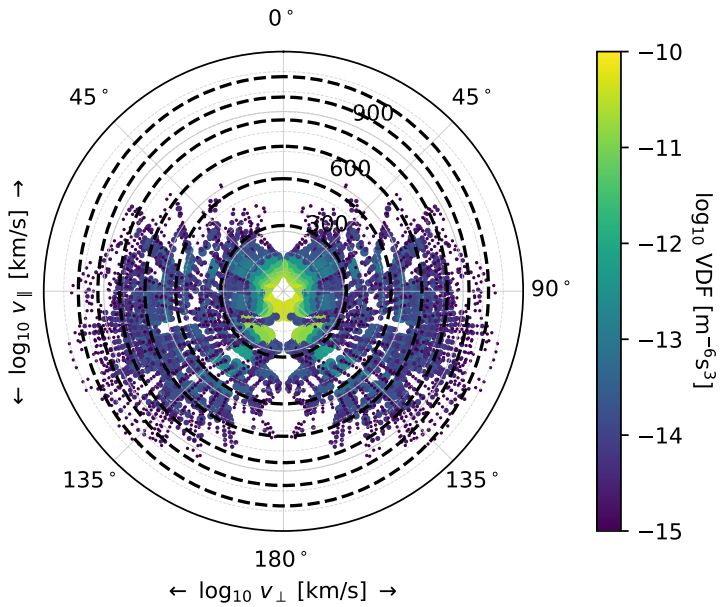

Figure 3. Collapsed velocity distribution calculated using the VDF shown in Figures 1 and 2. The magnetic field **B** can be imagined pointing toward the top. Observable pitch angles reach from 0° (parallel to **B**) over 90° (perpendicular to **B**) to 180° (antiparallel to **B**). As this would only cover half a polar plot, the same dataset is displayed on both the left and right halves to improve visibility. The shape of the successful 2D Maxwellian fit is indicated with black dashed contour lines.

4.4 Handling the limited resolution

It is important to note that a data*point* in the collapsed velocity distribution is by no means properly described as such. It can rather be described by a *box*, bounded by the azimuth and elevation apertures as well as the inherent uncertainty of the particle energy/velocity measurement. If one such box is far away from the center of the collapsed velocity distribution, the pitch angle range which it covers is quite small. If, however, the size of this box is kept constant and the box is moved close to the center (this is what happens to some datapoints/boxes when we shift the VDF to a plasma fixed frame), it may cover a very large range of pitch angles as illustrated in Figure 4. Three "data boxes", describing the coverage of three measurements in velocity space, are shown in Figure 4a-b. After shifting this exemplary distribution such that the bulk velocity lies in the center of the coordinate system, **B** already points along Z which supersedes a rotation of the bulk plasma reference frame. If all the corner points of a box are then projected into a collapsed velocity distribution (see Fig. 4c), we obtain the pitch-angular coverage each "data box" corresponds to. In this case, the flux represented by the blue bin covers a variety of different pitch angles as it is very close to the bulk velocity, it therefore was removed before a Maxwellian fit was performed. We remove all data points whose pitch angle uncertainty is larger than 45°.

4.5 Judging the goodness of fit

There are a number of reasons for poor fitting to occur: Not all VDFs are expected to be well approximated by a Maxwellian, as for example double-streaming or turbulent plasma can exhibit differently shaped VDFs. Even with a Maxwellian-shaped VDF, it can be difficult to get a reliable fit for numerical reasons e.g. when the VDF is unfavourably

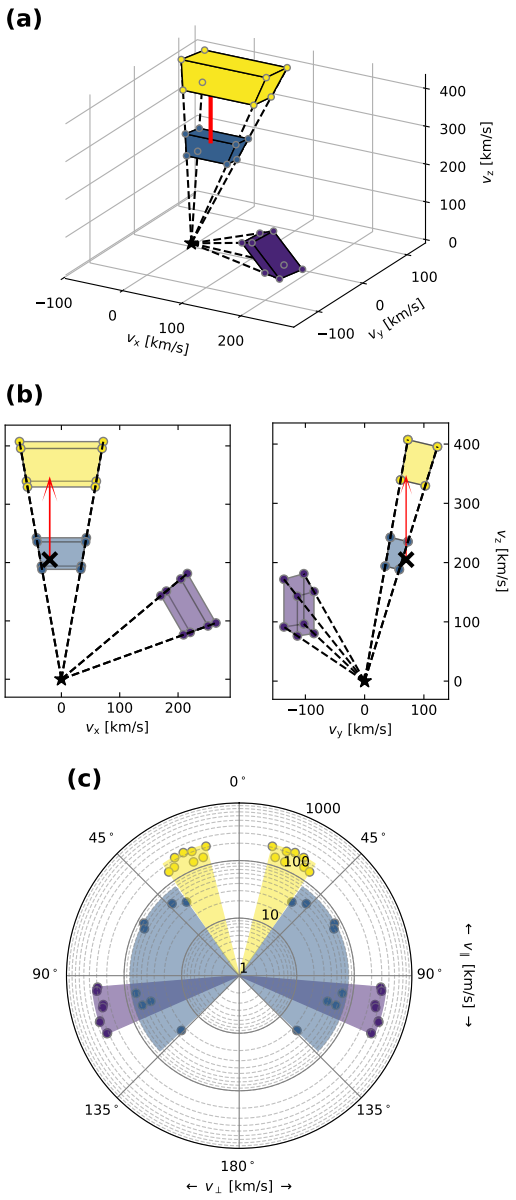

Figure 4. (a-b) Three typical "data boxes" in the initial VEX reference frame. A black star marks the center of the coordinate system while the black cross marks the bulk velocity. The red arrow marks the direction of the magnetic field **B**, for reasons of simplicity chosen to point along the *Z*-axis. (c) Resulting collapsed distribution of all boxes' corner points.

sampled by IMA, when the bulk flow is not in IMA's field of view, or when the total particle flux is too low. Lastly, sometimes the fitting procedure does not converge within the given iteration limit for the fitting procedure. In all these cases we want to remove the unsuitable distribution from our statistical analysis.

We validate the results of the two fitting steps described in Equations (2) and (3) as follows: We first require that the fitting procedure converged within the empirically given iteration limit. We then perform a boundary check where obviously bad parameter estimates (e.g., $v_{\mathrm{bulk}} > 1000\,\mathrm{km/s}$ or $T > 700\,\mathrm{eV}$), are removed. Only for the fitted parallel temperature $T_{\parallel}$ we require that its value can not change too quickly between two consecutively measured distributions. This removes spurious outliers where $T_{\parallel}$ is poorly constrained due to limited angular coverage near the magnetic field direction **B**. We also remove cases where the estimated bulk and thermal velocities are both less than 20 km/s at the same time as such cases can not be reliably measured by IMA due to its lower energy limit. Lastly, we use the modified index of agreement d_1 [*Legates and McCabe*, 1999] to judge the fit quality. d_1 is a better goodness of fit parameter than e.g. the coefficient of determination R^2 because the latter is also large when the fit is a arbitrary linear function of the data instead of the desired close identity. We assume that our collapsed velocity distribution with the observed probability density values O has been fitted such that we obtained corresponding fitted model values P. The modified index of agreement is d_1 defined as

$$d_1 = 1.0 - \frac{\sum_{i=1}^{N} |O_i - P_i|}{\sum_{i=1}^{N} \left(\left| P_i - \overline{O} \right| + \left| O_i - \overline{O} \right| \right)}. \tag{4}$$

The value of d_1 is in the range of 0 to 1 and increases with increasing goodness of fit. The selection criterion for d_1 below which the fit is discarded has been chosen defensively, as a small number of bad fits remaining in the dataset will be evened out by our averaging procedure at a later point anyway without noticeably impacting the results. Using an empirically chosen lower limit of $d_1 = 0.65$ for both the bulk velocity and proton temperature fits, about 82% of all proton VDFs in the solar wind and magnetosheath pass the acceptance filter and contribute to our results. In the magnetotail only about 40% of the VDF fits pass. This is also where most VDFs with both a low bulk velocity and a low temperature occur. In addition, VDFs in the magnetotail often don't correspond to a Maxwellian shape and our analysis method is not fully suitable for this region.

4.6 Creating maps

The calculated fit parameters are sorted into spatial bins using the VSO reference frame, which was described in section 3. We use a cylindrical coordinate system with X_{VSO} pointing toward the sun and oriented along the cylinder, and $R_{\mathrm{VSO}} = \sqrt{Y_{\mathrm{VSO}}^2 + Z_{\mathrm{VSO}}^2}$ describing the distance from the sun-Venus-line. This choice means that we assume a cylindrical symmetry around X_{VSO}. To justify this assumption we initially binned the data into four quadrants in the plane perpendicular to the X_{VSO}-axis. With a size of 90° each, the quadrants were centered around the $\pm Y_{\mathrm{VSO}}$ and $\pm Z_{\mathrm{VSO}}$ axes, representing the dawn/dusk and north/south directions in the VSO frame. We did not observe any asymmetries, largely due to the severely decreased number of samples per bin and increased noise, hence the binning into quadrants was removed to improve statistics. The bin size in X_{VSO} and R_{VSO} directions is $0.2 \times 0.2\,R_{\mathrm{V}}^2$; the region of interest is limited to $-3\,R_{\mathrm{V}} \leq X_{\mathrm{VSO}} \leq 2\,R_{\mathrm{V}}$ and $R_{\mathrm{VSO}} \leq 3.4\,R_{\mathrm{V}}$.

We bin proton bulk velocities, parallel and perpendicular temperatures separately. Average values for each bin are calculated using medians to minimize the impact of bad fits which might have made it through the acceptance filter. The average temperature ratio $T_\perp/T_\parallel$ is obtained by first computing the ratio for each individual VDF (each 192 s measurement) before taking the median value of all such temperature ratios in each spatial bin.

4.7 Instrumental effects and spacecraft charging

The angular resolution of IMA is defined by the 16 azimutal sectors and the step size in elevation direction. An individual instrument pixel is 22.5 deg x 4.5 deg in angular size. This elongated angular size translates to a direction dependent resolution in velocity space and results in a direction dependent lower limit for the temperature that can be determined from the data. This could be an issue especially for the angular narrow solar wind beam.

By running our fitting algorithm on modelled Maxwellian VDFs we verified that at average solar wind bulk velocities (400 km/s), proton temperatures down to 6 eV can be resolved very reliably even though the solar wind peak covers only few VDF bins in IMA. This is because the fitting is mostly controlled by the flanks of the VDF peak and not the actual peak itself. As the bulk velocity decreases, the situation improves as the sampling in velocity space is getting more dense.

Due to the varying orientations of the magnetic field B and the spacecraft - the lower resolving IMA azimuth direction is more or less randomly oriented in the frame where the anisotropy is fitted. This may occasionally result in an overestimation of either $T_\perp$ or $T_\parallel$, resulting in an additional spread in the distribution of the observed anisotropies. Careful inspection of individual fits shows that this additional spreading is suppressed by proper selection using the modified index of agreement described in section 4.5.

More frequent bad fitting may also occur for very low temperatures when the bulk flow approaches the lower limit of IMA's energy range; such cases are generally rejected by the fitting procedure however. Nevertheless, this may create a bias and lead to poorer statistics mostly in the magnetotail as noted in section 4.5.

We also investigated the influence of a possible calibration-related shift in the energy scale of IMA and of the spacecraft potential on our results. A shift of the energy calibration by -16.7 eV proposed by the instrument team did not significantly change the results besides slightly lowering the estimated bulk velocities as expected. The spacecraft potential on Venus Express is not measured directly and estimated using models [*Garrett*, 1981] to be of the order of ±5 V. An analysis of data corrected by an assumed spacecraft potential of this order did not produce significantly different results however, thus no corrections for spacecraft potential or IMA energy scale calibration were used in this study.

5 Results and discussion

5.1 Statistical temperatures

First we look at the spatial distribution of the perpendicular and parallel temperatures. The number of IMA scans in each spatial bin that is used to compute the average temperatures is shown in Figure 5a, the median bulk velocity and direction per bin in Fig. 5b. Bins with less than 10 usable VDFs are not shown. Assuming cylindrical symmetry and summing over all quadrants as explained in section 4.6, the orbit of Venus Express provides good coverage of the area of interest with more than 50-100 VDFs in most bins. Only the subsolar region close to Venus and parts of the magnetotail are not covered.

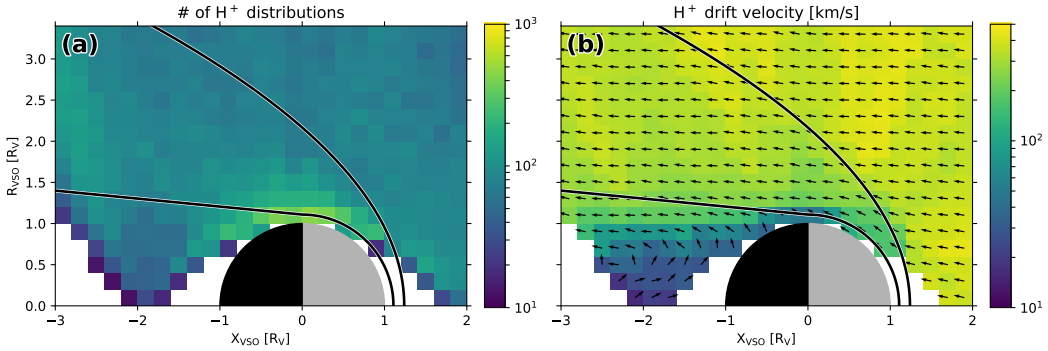

Figure 5. (a) The number of successfully fitted IMA scans used in this study, logarithmic color scale. Cylindrical symmetry is assumed and X_{VSO}-R_{VSO} coordinates are used. Venus is shown as a half gray and half black colored circle, representing day- and nightside respectively; the sun is located to the right of the plot. Units on the X and R axes are in Venus radii. White bins correspond to locations without sufficient coverage. The average bow shock [*Whittaker et al.*, 2010] and IMB [*Martinecz et al.*, 2008] positions are indicated with black lines. (b) Median bulk velocities, logarithmic color scale. The flow direction in each bin is indicated with black arrows.

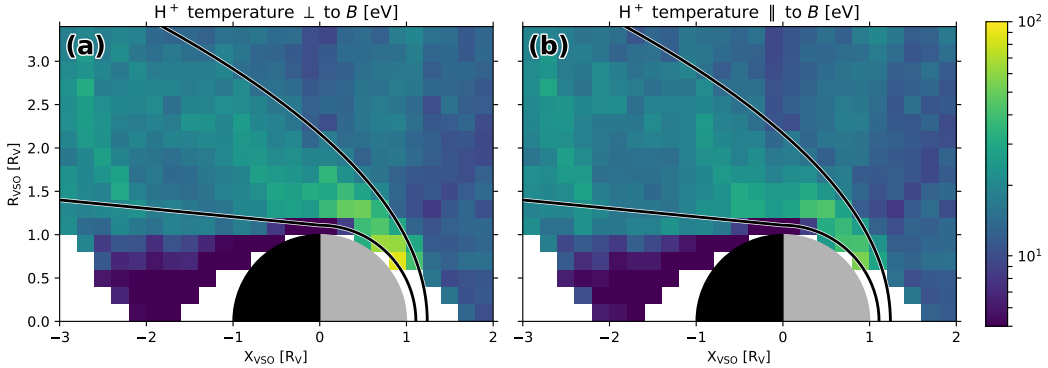

Figure 6. Proton temperatures (a) perpendicular and (b) parallel/antiparallel to the magnetic field.

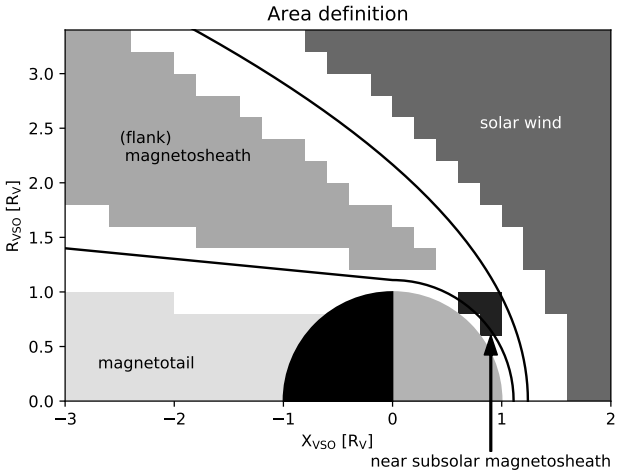

Figure 7. Definition of the solar wind, (flank) magnetosheath, magnetotail and near subsolar magnetosheath in X_{VSO}-R_{VSO} coordinates as used for the calculation of average values.

Table 1. Median proton plasma parameters and their median absolute deviations in the solar wind, magnetosheath, magnetotail and near subsolar magnetosheath

	v_{bulk} [km/s]	$T_\perp$ [eV]	$T_\parallel$ [eV]	$T_\perp/T_\parallel$ ratio
Solar wind	375 ± 64	13.0 ± 6.2	12.9 ± 6.1	1.00
(Flank) magnetosheath	307 ± 54	21.4 ± 10.8	20.5 ± 10.0	1.03
Near subsolar magnetosheath	160 ± 35	64.7 ± 36.1	41.3 ± 21.6	1.56
Magnetotail	37 ± 20	5.6 ± 3.5	5.6 ± 3.4	0.99

The proton temperatures perpendicular and parallel to the magnetic field are shown in Figure 6. We note a rather clear difference between the solar wind region and the magnetosheath; both the perpendicular and the parallel temperatures increase noticeably at the bow shock. Temperatures are highest close to the planet in the subsolar region, where also the perpendicular temperature seems to be larger than the parallel. The magnetotail region exhibits proton temperatures significantly lower than in the solar wind and magnetosheath.

We computed and compared the proton average temperatures and average bulk velocities for different regions in Venus' plasma environment. These regions, shown in Figure 7, are the solar wind, the flank magnetosheath (simply referred to as "magnetosheath" throughout the remainder of this paper) and the magnetotail. We furthermore separately consider the near subsolar magnetosheath, which is comprised of bins in the dayside magnetosheath where the solar wind pressure is expected to be highest. The average bow shock [*Whittaker et al.*, 2010] and IMB [*Martinecz et al.*, 2008] locations were used as approximate boundaries. We then omitted the bins closest to the nominal boundaries, as the boundary positions are not stationary but vary with time and bins close to either of the nominal boundaries are likely to include measurements from both sides of it. The omitted bins show up as white areas in Figure 7.

The average proton bulk velocity v_{bulk}, temperatures $T_\perp$ and $T_\parallel$ and the temperature ratio $T_\perp/T_\parallel$ in each region are calculated by averaging the corresponding parameters of all single VDFs without any prior spatial averaging. The resulting average values might therefore be spatially biased to some degree, but considering the relatively even spacecraft coverage shown in Figure 5 this impact should be minimal. Calculating an average from the spatially binned average values shown in Figure 6 was considered, but gives unrea-

sonably high weights to VDFs in bins with less coverage. However, the difference in the result using the two approaches is very small anyway.

Table 1 shows the resulting average proton bulk velocities and temperatures and their respective uncertainties, as well as the temperature ratios. Uncertainties are given as median absolute deviation (MAD), since all averaging is done using medians. The MAD of a dataset $\{x_i\}$ is calculated by

$$\mathrm{MAD} = \mathrm{median}(\ |x_i - \mathrm{median}(\{x_i\})|\ ). \tag{5}$$

The median perpendicular (parallel) temperature in the solar wind region is found to be 13.0 eV (12.9 eV) - significantly above the lower temperature resolution limit of IMA (see section 4.7). Close to 1 AU a recent statistical study using 10 years of data from the Wind spacecraft [*Wilson III et al.*, 2018] yielded a median (mean) solar wind proton temperature of 8.7 (12.7) eV and a greater parallel temperature compared to the perpendicular. However, the proton temperatures are found to decrease with radial distance from the sun and the perpendicular temperature decreases faster than the parallel. Hence, the temperature ratio $T_\perp/T_\parallel$ also decreases as one moves further out in the solar system [*Marsch et al.*, 1982]. Moreover, proton VDFs in the solar wind are often not simple Maxwellians. They may show a core distribution with $T_\perp/T_\parallel > 1$ together with a tail along the magnetic field or even a separate parallel beam [*Marsch et al.*, 2006]. The VDFs are also highly variable in time and space. For example, the details of the proton VDF depend on whether it resides in a slow or fast solar wind stream [*Feldman et al.*, 1973a,b]. Our analysis does not capture such variations or details of the VDFs but gives only an average mainly for the core distribution in those cases where a Maxwellian fit to the observed VDF converges and the goodness of fit criteria (Section 4.5) are fulfilled, which is true for 77% of all available scans in the solar wind.

Upon passing the bow shock and flowing into the magnetosheath, the proton perpendicular (parallel) temperature increases to reach 21.4 eV (20.5 eV) as the solar wind is forced to decelerate - and although the heating $\perp$ **B** is slightly stronger than $\parallel$ **B**, the distribution is still fairly isotropic. We expect heating to take place in the shock, although observations at the Earth's bow shock indicate that solar wind beams sometimes pass it with very little or no heating at all [*Parks et al.*, 2016]. On average, however, the plasma is heated and from theory we expect a greater perpendicular than parallel heating at a quasi-perpendicular shock, while the parallel heating should be greater behind a quasi-parallel shock [*Halekas et al.*, 2017, and references therein]. In this study we did not distinguish between different types of shocks in order to improve our statistics and we see that on average the perpendicular heating is slightly larger. In the near subsolar magnetosheath where the heating is expected to be strongest, we find much larger temperatures of on average $T_\perp = 64.7$ eV and $T_\parallel = 41.3$ eV. We will have a closer look at this obvious $T_\perp/T_\parallel > 1$ anisotropy and its implications for low-frequency wave generation in the following sections.

In the magnetotail we observe very low temperatures of only ≈ 6 eV. Most plasma in this region is of planetary origin [*Nordström et al.*, 2013] and consists of planetary protons and Helium ions together with heavier ions like O_2^+ and O^{2+}. The planetary ions are gradually accelerated to escape energies throughout the tail. At Mars studies have shown that a low energy tailward drifting component is dominating large parts of the tail [*Nilsson et al.*, 2012]. The situation in Venus' magnetotail is complicated as there is a substantial flow of ions returning toward Venus [*Kollmann et al.*, 2016; *Persson et al.*, 2018]. In our study the algorithm to find the bulk velocity chooses the dominant peak of the distribution and the temperatures computed are then associated with this peak. One should note though that very often a bi-Maxwellian distribution is not a good choice to describe the VDFs in this region. Furthermore, distributions that have at the same time low temperatures and a low bulk velocity are not well sampled by IMA because of the rather coarse energy stepping of the instrument at energies below a few 10s eV/q and due to the uncertainty in the en-

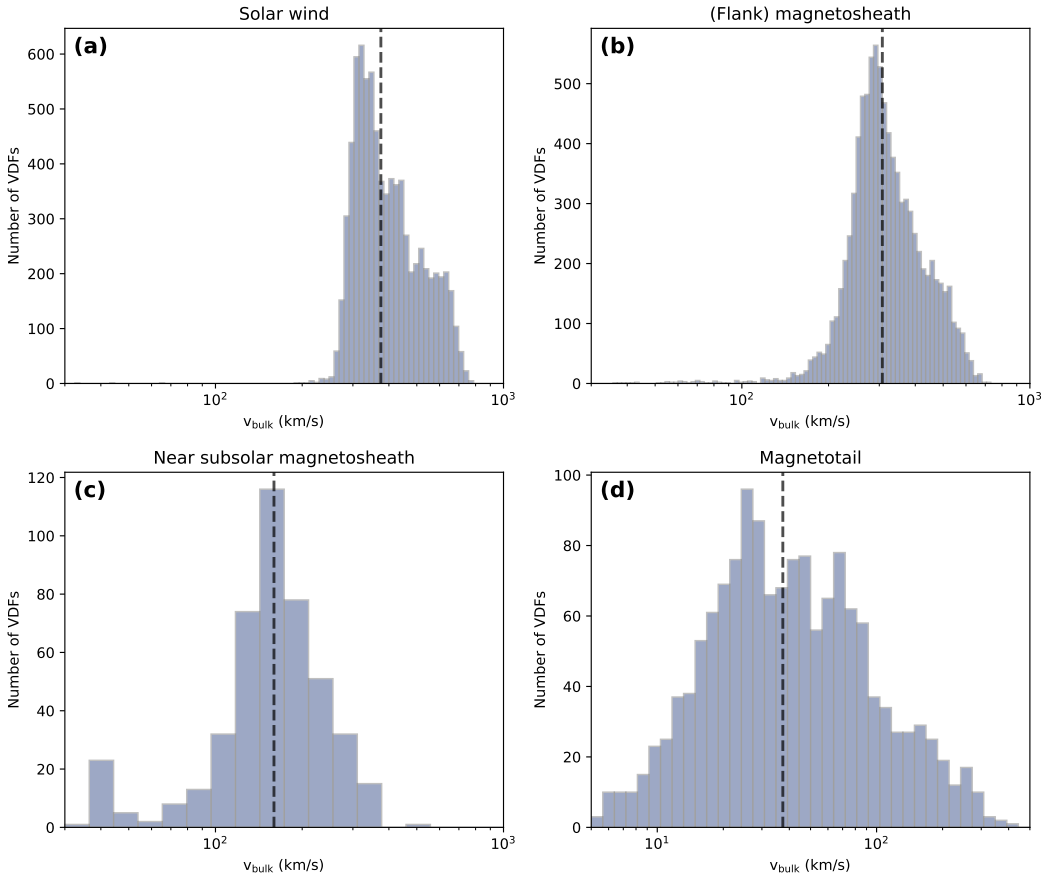

Figure 8. Histograms of fitted drift velocities in (a) the solar wind, (b) the (flank) magnetosheath, (c) the near subsolar magnetosheath and (d) the magnetotail as defined in Figure 7. The bin size and shown range have been chosen to fit the number of measurements and their distribution, note the different velocity scale in panel (d). Dashed vertical lines mark the median values noted in Table 1.

ergy scale as described in section 4.7. Only for 40% of the scans observed an accepted bi-Maxwellian fit is found. The accepted fits in this region are expected to have a bias toward higher values of $T_\perp$, $T_\parallel$ and $v_{\rm bulk}$.

In Figures 8 to 10 we present histograms of the proton bulk velocity, the perpendicular and parallel temperatures and the the temperature ratio $T_\perp/T_\parallel$, separated into the regions defined above.

The bulk velocity in the solar wind (see Fig. 8a) ranges from about 250 km/s to 700 km/s, with $\sim$ 375 km/s as the median speed observed. The solar wind distribution looks as if comprised of three different distributions with different median speeds. Moving into the magnetosheath (8b), the drift velocity decreases to 200-600 km/s and the structure seen in the solar wind velocity distribution is smeared out. Otherwise the magnetosheath distribution very much resembles the solar wind distribution. In the near subsolar magnetosheath (8c) the velocity decreases more significantly and in the magnetotail the bulk flows generally stay below 100 km/s (8d).

The distributions of the perpendicular (blue) and parallel (yellow) proton temperatures are shown in Fig. 9. The temperatures appear lognormal-distributed except perhaps in the near subsolar magnetosheath. Solar wind observations close to Earth [e.g., *Burlaga*

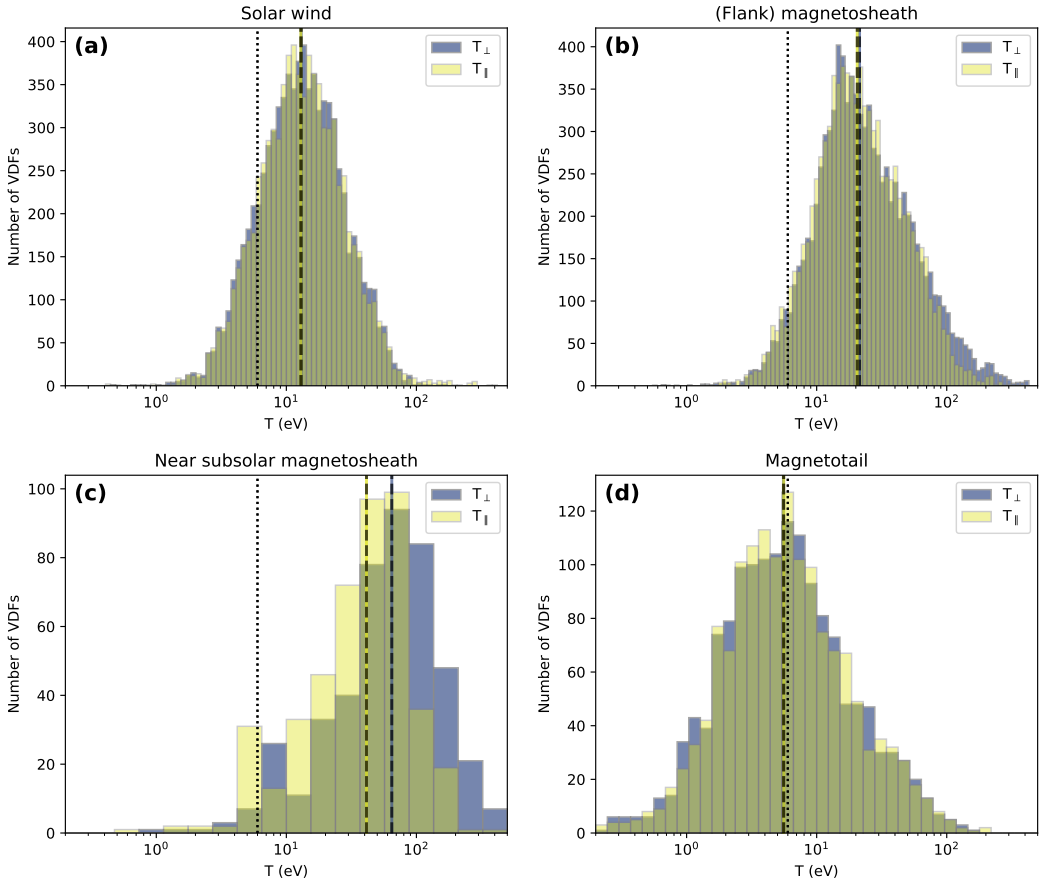

Figure 9. Histograms of fitted $T_{\perp}$ (blue) and $T_{\parallel}$ (yellow) values, same format as Figure 8. An empirically determined upper limit to the detectable temperature threshold is shown with a dotted line, left of which the reliability of the temperature estimation decreases due to the angular resolution of the instrument.

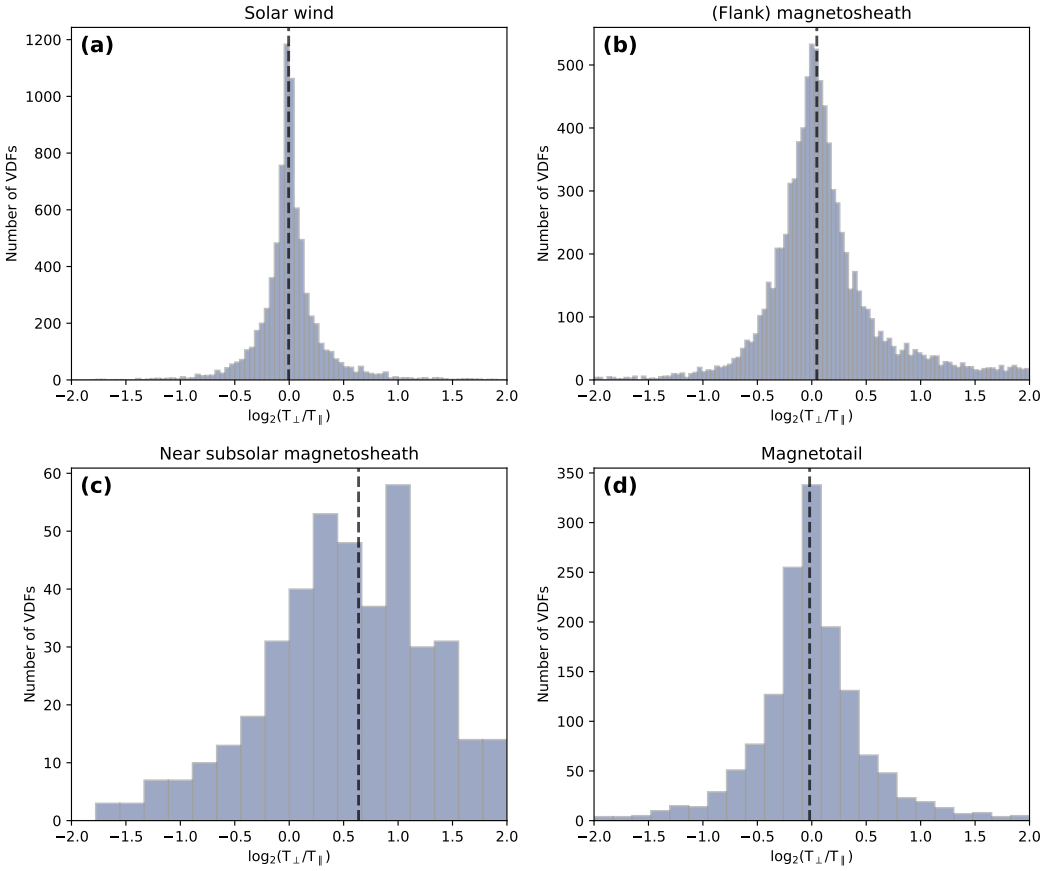

Figure 10. Histograms of fitted $T_\perp/T_\parallel$ ratios, same format as Figure 8. Note the binary logarithmic scale on the horizontal axis.

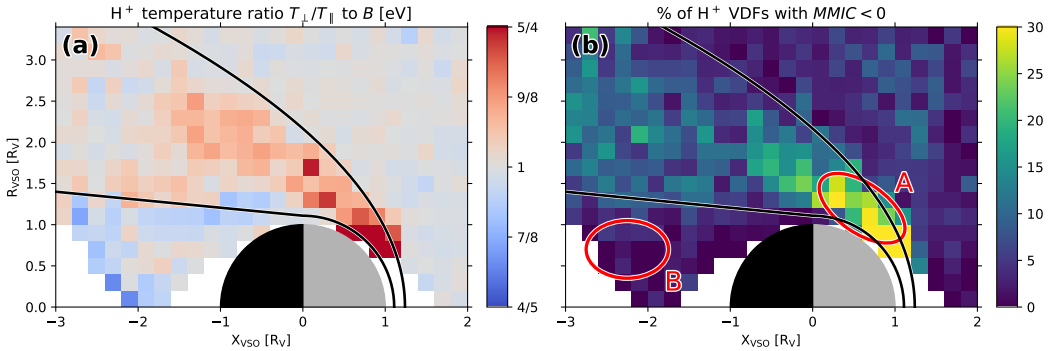

Figure 11. (a) Proton temperature ratio $T_\perp/T_\parallel$ around Venus in X_{VSO}-R_{VSO} coordinates. The color scale has been adjusted such that for example a ratio of 5/4 is displayed in red with the same color intensity as its inverse value 4/5 in blue. (b) Percentage of VDFs which fulfilled the proton MM instability criterion, in X_{VSO}-R_{VSO} coordinates. The red ellipse A marks the approximate area where *Volwerk et al.* [2008b] found strongly enhanced MM wave activity in the dayside magnetosheath. The second red ellipse B approximately marks a region where reduced, but also higher than expected MM wave activity was observed.

et al., 1999; *Burlaga and Lazarus*, 2000; *Wilson III et al.*, 2018] also show a log-normal distribution of proton temperatures. The distribution shifts to higher temperatures inside the magnetosheath (9b) and becomes slightly more skewed, exhibiting a tail toward higher temperatures. In both cases the perpendicular and the parallel temperature distributions have the same shape. Temperatures found in the near subsolar magnetosheath (9c) are comparable to the high-$T_\perp$ tail in the magnetosheath, reaching some hundreds of eV. Here the difference between the perpendicular and parallel temperatures is obvious. The $T_\perp$ and $T_\parallel$ distributions in the magnetotail (9d) also seem to follow lognormal shapes but the protons here are much colder than in the other three regions.

Figure 10 shows histograms of the proton temperature ratios $T_\perp/T_\parallel$, with the horizontal axis adjusted such that, e.g., $T_\perp/T_\parallel = 4$ and $T_\perp/T_\parallel = 1/4$ are symmetric around $T_\perp/T_\parallel = 1$. In the solar wind (10a) we observe a narrow peak centered on $T_\perp = T_\parallel$, indicating largely isotropic distributions. The sharp peak broadens and slightly shifts to $T_\perp > T_\parallel$ in the magnetosheath (10b). The dayside region (10c) is clearly dominated by perpendicular heating. In the magnetotail (10d) $T_\perp$ is slightly less than $T_\parallel$ on average but the distribution seems very symmetric.

5.2 Statistical temperature ratios

Figure 11a shows a map of the proton temperature ratio $T_\perp/T_\parallel$ in X_{VSO}-R_{VSO} coordinates. Median values for different regions around Venus (obtained without any prior spatial averaging) are found in Table 1.

In the solar wind we generally observe temperature ratios very close to $T_\perp/T_\parallel = 1$, as was discussed in the previous section. The histogram in Figure 10a shows a narrow peak at $T_\perp = T_\parallel$. The ratio $T_\perp/T_\parallel$ increases at the bow shock. The median ratio is not significantly different from 1, but we note that the ratio is consistently larger than 1 throughout most of the magnetosheath. In a simplified picture, the generation of a temperature/pressure anisotropy can be considered an effect of magnetic field compression and plasma depletion along a plasma streamline, and is theoretically described by [*Crooker and Siscoe*, 1977]

$$\frac{p_\perp}{p_\parallel} = \left(\frac{\rho_0}{\rho}\right)^2 \left(\frac{B}{B_0}\right)^3. \quad (6)$$

For a quasi-parallel shock one expects less magnetic field amplification and therefore a greater parallel heating while the opposite would be the case for a quasi-perpendicular shock. In a particle view the heating is the result of the reflection of some of the incident ions at the bow shock. In quasi-perpendicular shock conditions ($\theta_{\mathrm{Bn}} > 45°$, with θ_{Bn} as the as the angle between the upstream magnetic field B_{IMF} and the local shock normal), the guiding center motion of a specularly reflected ion is directed downstream. The reflected ions have a strongly increased temperature and eventually gyrate through the bow shock, where they contribute to a stronger perpendicular than parallel heating. The proton temperature ratio therefore increases to average values of $T_\perp/T_\parallel > 1$. In the near subsolar magnetosheath where the interaction with Venus' induced magnetosphere is strongest, we frequently observe perpendicular temperature anisotropies with $T_\perp/T_\parallel > 2$ (see Fig. 10c). The average ratio here is $T_\perp/T_\parallel \approx 3/2$ (see Table 1). Good summaries of this mechanism and related observations at the Earth's bow shock are for example given in *Gosling and Robson* [1985] and *Sckopke et al.* [1990].

In our analysis we do not distinguish between different shock geometries, the statistical $T_\perp > T_\parallel$ anisotropy could hence be a consequence of a dominance of quasi-perpendicular shock crossings in the data set. Moreover, from observations on Earth we know that the ratio $T_\perp/T_\parallel$ increases as one moves from the bow shock toward the magnetopause [*Dimmock et al.*, 2015]. As the VEX spacecraft moves fast close to the planet and hence one observation corresponds to a fairly large distance, that means the observed VDF will be an average over a large distance in the magnetosheath. *Halekas et al.* [2017] also on average observes a $T_\perp/T_\parallel > 1$ anisotropy in the magnetosheath of Mars, although they show in a case study a greater parallel heating occurring at a quasi-parallel bow shock.

The proton distributions are observed to become more isotropic as the plasma flows downstream past Venus. This can likely be attributed to the generation of low-frequency waves which serve to transfer energy between different proton populations and stabilize the downstream distributions. The same tendency is observed at Mars [*Halekas et al.*, 2017].

Close to the nightside IMB and in the magnetotail we observe bins with a slight $T_\perp < T_\parallel$ anisotropy. In fact the IMB appears as a clearly defined transition in Fig. 11a. This may not be surprising considering that the IMB seems to separate ionospheric ions from solar wind ions rather well on Venus judging from Figures 7-9 in *Nordström et al.* [2013]. The proton population in the tail may therefore be almost entirely of ionospheric origin. One would not have been surprised though if this population had shown signs of perpendicular heating, due to for example wave-particle interaction, and it would be of interest for future studies to compare proton VDFs with VDFs of heavy ions in the tail.

5.3 Wave generation

A $T_\perp/T_\parallel > 1$ anisotropy may generate waves. Proton cyclotron waves and mirror mode waves are both unstable to such an anisotropy and they are both observed in the environment around Venus.

The proton cyclotron waves observed in Venus' magnetosheath are usually assumed to be generated by an unstable ring-beam distribution caused by the pickup of exospheric hydrogen as is the case at Mars [*Russell et al.*, 2006a]. However, Figs. 10 and 11a shows that $T_\perp/T_\parallel > 1$ is often true in the magnetosheath and the temperature anisotropy provides an alternative generation mechanism for proton cyclotron waves here. The importance of different generation processes is still to be investigated.

Waves near the local proton cyclotron frequency are also observed in the solar wind upstream of Venus [*Delva et al.*, 2008a, 2011; *Wei et al.*, 2011], but their origin is still debated. *Delva et al.* [2011] argues that they are the result of exospheric hydrogen reaching far beyond the bow shock which is being picked up by the solar wind. *Wei et al.* [2011]

on the other hand suggests that the observed waves are most likely a consequence of ions back-streaming from the parallel shock or generated closer to the sun and transported to the observation location. Our observations show a mainly isotropic proton distribution in the solar wind providing no alternative source of proton cyclotron waves in this region.

Mirror mode (MM) waves have been found in the vicinity of several planets, e.g., in the magnetosheath of the Earth [e.g., *Baumjohann et al.*, 1999; *Lucek et al.*, 1999; *Constantinescu et al.*, 2003], and Mars [*Bertucci et al.*, 2004]. With the beginning of Venus Express' science phase, *Volwerk et al.* [2008a,b] observed mirror-mode-like structures in the magnetosheath of Venus. They were later shown to be nearly independent of the solar cycle [*Volwerk et al.*, 2016].

The MM instability criterion for a bi-Maxwellian plasma is given by

$$MMIC = 1 + \beta_{\perp}\left(1 - \frac{T_{\perp}}{T_{\parallel}}\right) < 0, \tag{7}$$

with

$$\beta_{\perp} = \frac{nk_{\mathrm{B}}T_{\perp}}{B^2/2\mu_0} \tag{8}$$

as the ratio of plasma pressure to the magnetic field pressure in the perpendicular direction. Here n denotes the proton number density, k_{B} the Boltzmann constant, B the local magnetic field strength and μ_0 the permeability of free space [*Hasegawa*, 1969]. We note that a temperature anisotropy is the only likely generation mechanism for MM waves, and the interest in MM wave observations is less the mechanism of their generation but rather the origin of the generating temperature anisotropy [*Ala-Lahti et al.*, 2018].

The MM waves observed in the Venusian magnetosheath were shown to have periods of $4 \leq T \leq 15$ s [e.g., *Volwerk et al.*, 2008a]. This means that ion data from IMA cannot be used for a direct identification of MM waves due to its low time resolution (192 s cadence). We can however calculate for each IMA scan whether the instability criterion is fulfilled; this way we can estimate whether conditions are statistically favorable for MM wave generation in different regions. A map showing the percentage of scans in each spatial bin during which the proton MM instability criterion was fulfilled is shown in Figure 11b.

Throughout most of the magnetosheath, the instability criterion is fulfilled during at least 10% of scans per bin. The highest probability of encountering MM instabilities is in the dayside magnetosheath, close to Venus where thermal pressure and temperature anisotropies are highest. In the near subsolar magnetosheath, as defined in the previous sections, probabilities above 30% are observed.

Conditions in the solar wind seem unfavorable for the generation of MM waves due to a low $\beta_{\perp}$ and highly isotropic distributions. In spite of this, mirror mode-like structures are observed in the solar wind upstream of Venus' bow shock [*Zhang et al.*, 2008b]. However, it is not clear whether they are generated by the mirror instability. In the solar wind the mirror mode structures take the form of magnetic holes, that is, isolated intervals with a depressed magnetic field, and soliton theory can alternatively be used to explain their existence [*Baumgärtel*, 1999; *Sperveslage et al.*, 2000].

Areas with enhanced MM wave activity found by *Volwerk et al.* [2008b] are marked with the red ellipses in Fig. 11b. They found that MM wave events were most likely to be observed in the dayside magnetosheath (region A), and that the events in this area were also the most intense. This fits well to our observations which suggest that the MM instability criterion is fulfilled most frequently in this region; the mirror mode waves detected here are hence almost certainly generated by the temperature anisotropy. *Volwerk et al.* [2008b] also detected mirror mode waves in the magnetotail, where according to our investigations the instability criterion is fulfilled only rarely. More detailed studies using both field and particle data would be needed to verify that the observed magnetic field

structures are true mirror modes and to compare with the particle distributions observed simultaneously. Unfortunately the time resolution of the ion measurements done by Venus Express is not high enough to do this. One should also keep in mind that a bi-Maxwellian description of the VDFs is often not good enough in the magnetotail.

6 Conclusions

Using VEX ion measurements between May 2006 and December 2009, we obtain average proton temperatures and temperature ratios in the Venus plasma environment ranging from $2\,R_V$ upstream to $3\,R_V$ downstream of Venus.

We observe highly isotropic proton distributions upstream of the bow shock, with both parallel and perpendicular temperatures of about 13 eV; upon passing the bow shock, the protons are heated to temperatures about 20 eV. On average, the VDFs in the magnetosheath are slightly anisotropic with $T_\perp > T_\parallel$ but the median ratio is still very close to 1. In the dayside magnetosheath where the compression of Venus' induced magnetosphere is strongest, the heating is larger compared to the rest of the magnetosheath. The temperature anisotropy here is pronounced with on average $T_\perp/T_\parallel \approx 3/2$ and temperatures of up to 65 eV (perpendicular). In the magnetotail we observe low energy protons of planetary origin that are almost isotropic.

A plasma with a perpendicular temperature anisotropy $T_\perp > T_\parallel$ may be unstable to both proton cyclotron and mirror mode waves, and both wave modes occur close to Venus. Proton cyclotron waves are observed in the magnetosheath where we indeed find $T_\perp/T_\parallel$, but they are normally attributed to the pickup of exospheric hydrogen creating an unstable ring-beam distribution. From our observations we argue that the proton temperature anisotropy in the dayside magnetosheath is an additional source of proton cyclotron waves.

Mirror mode waves were most frequently observed in the near subsolar magnetosheath, where the instability criterion is most often fulfilled. We conclude that the mirror mode waves observed here are a result of the observed proton temperature anisotropy.

Acknowledgments

All VEX data is publicly acccessible at the ESA Planetary Science Archive at `https://www.cosmos.esa.int/web/psa/venus-express`. AB acknowledges support from the Swedish Institute of Space Physics (IRF) during the initial stages of this project and is funded by a Lancaster University FST studentship. The work of G. Stenberg Wieser is supported by the Swedish National Space Board through grant 96/15.

References

Ala-Lahti, M. M., E. K. J. Kilpua, A. P. Dimmock, A. Osmane, T. Pulkkinen, and J. Souček (2018), Statistical analysis of mirror mode waves in sheath regions driven by interplanetary coronal mass ejection, *Annales Geophysicae*, *36*(3), 793–808, doi: 10.5194/angeo-36-793-2018.

Barabash, S., J.-A. Sauvaud, H. Gunell, H. Andersson, A. Grigoriev, K. Brinkfeldt, M. Holmström, R. Lundin, M. Yamauchi, K. Asamura, W. Baumjohann, T. L. Zhang, A. J. Coates, D. R. Linder, D. O. Kataria, C. C. Curtis, K. C. Hsieh, B. R. Sandel, A. Fedorov, C. Mazelle, J.-J. Thocaven, M. Grande, H. E. J. Koskinen, E. Kallio, T. Säles, P. Riihela, J. Kozyra, N. Krupp, J. Woch, J. Luhmann, S. McKenna-Lawlor, S. Orsini, R. Cerulli-Irelli, M. Mura, M. Milillo, M. Maggi, E. Roelof, P. Brandt, C. T. Russell, K. Szego, J. D. Winningham, R. A. Frahm, J. Scherrer, J. R. Sharber, P. Wurz, and P. Bochsler (2007), The Analyser of Space Plasmas and Energetic Atoms (ASPERA-4) for the Venus Express mission, *Planetary and Space Science*, *55*(12), 1772–1792, doi:10.1016/j.pss.2007.01.014.

Baumgärtel, K. (1999), Soliton approach to magnetic holes, *Journal of Geophysical Research: Space Physics*, *104*(A12), 28,295–28,308, doi:10.1029/1999JA900393.

Baumjohann, W., R. A. Treumann, E. Georgescu, G. Haerendel, K.-H. Fornaçon, and U. Auster (1999), Waveform and packet structure of lion roars, *Annales Geophysicae*, *17*, 1528–1534.

Bertucci, C., C. Mazelle, D. H. Crider, D. L. Mitchell, K. Sauer, M. H. Acuña, J. E. P. Connerney, R. P. Lin, N. F. Ness, and D. Winterhalter (2004), MGS MAG/ER observations at the magnetic pileup boundary of Mars: draping enhancement and low frequency waves, *Advances in Space Research*, *33*(11), 1938–1944, doi:10.1016/j.asr.2003.04.054.

Boggs, P., and J. Rogers (1990), Orthogonal Distance Regression, in *Statistical analysis of measurement error models and applications: proceedings of the AMS-IMS-SIAM joint summer research conference held June 10-16, 1989*, vol. 112, p. 186, Contemporary Mathematics.

Brain, D. A., F. Bagenal, M. H. Acuña, J. E. P. Connerney, D. H. Crider, C. Mazelle, D. L. Mitchell, and N. F. Ness (2002), Observations of low-frequency electromagnetic plasma waves upstream from the Martian shock, *Journal of Geophysical Research*, *107*(A6), 1076, doi:10.1029/2000JA000416.

Brain, D. A., F. Bagenal, Y.-J. Ma, H. Nilsson, and G. Stenberg Wieser (2016), Atmospheric escape from unmagnetized bodies, *Journal of Geophysical Research: Planets*, *121*(12), 2364–2385, doi:10.1002/2016JE005162.

Burlaga, L. F., and A. J. Lazarus (2000), Lognormal distributions and spectra of solar wind plasma fluctuations: Wind 1995-1998, *Journal of Geophysical Research: Space Physics*, *105*(A2), 2357–2364, doi:10.1029/1999JA900442.

Burlaga, L. F., A. Szabo, L. F. Burlaga, and A. Szabo (1999), Fast and Slow Flows in the Solar Wind near the Ecliptic at 1 AU?, *Space Science Reviews*, *87*, 137–140, doi:10.1023/A:1005186720589.

Colin, L. (1980), The Pioneer Venus Program, *Journal of Geophysical Research*, *85*(A13), 7575–7598, doi:10.1029/JA085iA13p07575.

Constantinescu, O. D., K.-H. Glassmeier, R. Treumann, and K.-H. Fornaçon (2003), Magnetic mirror structures observed by Cluster in the magnetosheath, *Geophysical Research Letters*, *30*(15), 1802, doi:10.1029/2003GL017313.

Crooker, N. U., and G. L. Siscoe (1977), A mechanism for pressure anisotropy and mirror instability in the dayside magnetosheath, *Journal of Geophysical Research*, *82*(1), 185–186, doi:10.1029/JA082i001p00185.

Delva, M., and E. Dubinin (1998), Upstream ULF fluctuations near Mars, *Journal of Geophysical Research: Space Physics*, *103*(A1), 317–326, doi:10.1029/97JA02501.

Delva, M., T. L. Zhang, M. Volwerk, W. Magnes, C. T. Russell, and H. Y. Wei (2008a), First upstream proton cyclotron wave observations at Venus, *Geophysical Research Letters*, *35*(L03105), doi:10.1029/2007GL032594.

Delva, M., T. L. Zhang, M. Volwerk, Z. Vörös, and S. A. Pope (2008b), Proton cyclotron waves in the solar wind at Venus, *Journal of Geophysical Research*, *113*(E00B06), doi:10.1029/2008JE003148.

Delva, M., C. Mazelle, C. Bertucci, M. Volwerk, Z. Vörös, and T. L. Zhang (2011), Proton cyclotron wave generation mechanisms upstream of Venus, *Journal of Geophysical Research: Space Physics*, *116*(A02318), doi:10.1029/2010JA015826.

Dimmock, A. P., A. Osmane, T. I. Pulkkinen, and K. Nykyri (2015), A statistical study of the dawn-dusk asymmetry of ion temperature anisotropy and mirror mode occurrence in the terrestrial dayside magnetosheath using THEMIS data, *Journal of Geophysical Research: Space Physics*, *120*(7), 5489–5503, doi:10.1002/2015JA021192.

Dubinin, E., M. Fraenz, J. Woch, T. L. Zhang, J. Wei, A. Fedorov, S. Barabash, and R. Lundin (2012), Bursty escape fluxes in plasma sheets of Mars and Venus, *Geophysical Research Letters*, *39*(L01104), doi:10.1029/2011GL049883.

Dubinin, E., M. Fraenz, T. L. Zhang, J. Woch, Y. Wei, A. Fedorov, S. Barabash, and R. Lundin (2013), Plasma in the near Venus tail: Venus Express observations, *Journal of Geophysical Research: Space Physics*, *118*(12), 7624–7634, doi:10.1002/2013JA019164.

Fedorov, A., S. Barabash, J.-A. Sauvaud, Y. Futaana, T. L. Zhang, R. Lundin, and C. Ferrier (2011), Measurements of the ion escape rates from Venus for solar minimum, *Journal of Geophysical Research: Space Physics*, *116*(A07220), doi:10.1029/2011JA016427.

Feldman, W. C., J. R. Asbridge, S. J. Bame, and M. D. Montgomery (1973a), Double ion streams in the solar wind, *Journal of Geophysical Research*, *78*(13), 2017–2027, doi:10.1029/JA078i013p02017.

Feldman, W. C., J. R. Asbridge, S. J. Bame, and M. D. Montgomery (1973b), On the origin of solar wind proton thermal anisotropy, *Journal of Geophysical Research*, *78*(28), 6451–6468, doi:10.1029/JA078i028p06451.

Fränz, M., E. Dubinin, E. Roussos, J. Woch, J. D. Winningham, R. Frahm, A. J. Coates, A. Fedorov, S. Barabash, and R. Lundin (2007), Plasma Moments in the Environment of Mars: Mars Express ASPERA-3 Observations, *Space Science Reviews*, *126*(1-4), 165–207, doi:10.1007/s11214-006-9115-9.

Fränz, M., E. Echer, A. Marques de Souza, E. Dubinin, and T. Zhang (2017), Ultra low frequency waves at Venus: Observations by the Venus Express spacecraft, *Planetary and Space Science*, *146*, 55–65, doi:10.1016/j.pss.2017.08.011.

Futaana, Y., G. Stenberg Wieser, S. Barabash, and J. G. Luhmann (2017), Solar Wind Interaction and Impact on the Venus Atmosphere, *Space Science Reviews*, *212*(3-4), 1453–1509, doi:10.1007/s11214-017-0362-8.

Garrett, H. B. (1981), The charging of spacecraft surfaces, *Reviews of Geophysics*, *19*(4), 577, doi:10.1029/RG019i004p00577.

Gary, S. P. (1992), The mirror and ion cyclotron anisotropy instabilities, *Journal of Geophysical Research*, *97*(A6), 8519, doi:10.1029/92JA00299.

Gosling, J. T., and A. E. Robson (1985), Ion reflection, gyration, and dissipation at supercritical shocks, in *Collisionless Shocks in the Heliosphere: Reviews of Current Research*, *Geophysical monograph series*, vol. 35, edited by B. T. Tsurutani and R. G. Stone, pp. 141–152, American Geophysical Union, Washington, D. C., doi:10.1029/GM035p0141.

Halekas, J. S., D. A. Brain, J. G. Luhmann, G. A. DiBraccio, S. Ruhunusiri, Y. Harada, C. M. Fowler, D. L. Mitchell, J. E. P. Connerney, J. R. Espley, C. Mazelle, and B. M. Jakosky (2017), Flows, Fields, and Forces in the Mars-Solar Wind Interaction, *Journal of Geophysical Research: Space Physics*, *122*(11), 11,320–11,341, doi:10.1002/2017JA024772.

Hasegawa, A. (1969), Drift Mirror Instability in the Magnetosphere, *Physics of Fluids*, *12*(12), 2642, doi:10.1063/1.1692407.

Kollmann, P., P. Brandt, G. Collinson, Z. Rong, Y. Futaana, and T. Zhang (2016), Properties of planetward ion flows in Venus' magnetotail, *Icarus*, *274*, 73–82, doi:10.1016/j.icarus.2016.02.053.

Legates, D. R., and G. J. McCabe (1999), Evaluating the use of "goodness-of-fit" Measures in hydrologic and hydroclimatic model validation, *Water Resources Research*, *35*(1), 233–241, doi:10.1029/1998WR900018.

Lucek, E., M. Dunlop, A. Balogh, P. Cargill, W. Baumjohann, E. Georgescu, G. Hearendel, and K.-H. Fornacon (1999), Mirror mode structures observed in the dawn-side magnetosheath by Equator-S, *Geophysical Research Letters*, *26*(14), 2159–2162.

Luhmann, J. (1986), The solar wind interaction with Venus, *Space Science Reviews*, *44*(3-4), doi:10.1007/BF00200818.

Marsch, E., K.-H. Mühlhäuser, R. Schwenn, H. Rosenbauer, W. Pilipp, and F. M. Neubauer (1982), Solar wind protons: Three-dimensional velocity distributions and derived plasma parameters measured between 0.3 and 1 AU, *Journal of Geophysical Research*, *87*(A1), 52, doi:10.1029/JA087iA01p00052.

Marsch, E., L. Zhao, and C.-Y. Tu (2006), Limits on the core temperature anisotropy of solar wind protons, *Annales Geophysicae*, *24*(7), 2057–2063, doi:10.5194/angeo-24-2057-2006.

Martinecz, C., M. Fränz, J. Woch, N. Krupp, E. Roussos, E. Dubinin, U. Motschmann, S. Barabash, R. Lundin, M. Holmström, H. Andersson, M. Yamauchi, A. Grigoriev, Y. Futaana, K. Brinkfeldt, H. Gunell, R. Frahm, J. Winningham, J. Sharber, J. Scherer, A. Coates, D. Linder, D. Kataria, E. Kallio, T. Sales, W. Schmidt, P. Riihela, H. Koskinen, J. Kozyra, J. Luhmann, C. Russell, E. Roelof, P. Brandt, C. Curtis, K. Hsieh, B. Sandel, M. Grande, J.-A. Sauvaud, A. Fedorov, J.-J. Thocaven, C. Mazelle, S. McKenna-Lawler, S. Orsini, R. Cerulli-Irelli, M. Maggi, A. Mura, A. Milillo, P. Wurz, A. Galli, P. Bochsler, K. Asamura, K. Szego, W. Baumjohann, T. Zhang, and H. Lammer (2008), Location of the bow shock and ion composition boundaries at Venus—initial determinations from Venus Express ASPERA-4, *Planetary and Space Science*, *56*(6), 780–784, doi:10.1016/j.pss.2007.07.007.

McEnulty, T., J. Luhmann, I. de Pater, D. Brain, A. Fedorov, T. Zhang, and E. Dubinin (2010), Interplanetary coronal mass ejection influence on high energy pick-up ions at Venus, *Planetary and Space Science*, *58*(14-15), 1784–1791, doi:10.1016/j.pss.2010.07.019.

Nilsson, H., G. Stenberg, Y. Futaana, M. Holmström, S. Barabash, R. Lundin, N. J. T. Edberg, and A. Fedorov (2012), Ion distributions in the vicinity of Mars: Signatures of heating and acceleration processes, *Earth, Planets and Space*, *64*(2), 135–148, doi:10.5047/eps.2011.04.011.

Nordström, T., G. Stenberg, H. Nilsson, S. Barabash, and T. L. Zhang (2013), Venus ion outflow estimates at solar minimum: Influence of reference frames and disturbed solar wind conditions, *Journal of Geophysical Research: Space Physics*, *118*(6), 3592–3601, doi:10.1002/jgra.50305.

Norqvist, P., M. André, and M. Tyrland (1998), A statistical study of ion energization mechanisms in the auroral region, *Journal of Geophysical Research: Space Physics*, *103*(A10), 23,459–23,473, doi:10.1029/98JA02076.

Parks, G. K., E. Lee, S. Y. Fu, H. E. Kim, Y. Q. Ma, Z. W. Yang, Y. Liu, N. Lin, J. Hong, P. Canu, I. Dandouras, H. Rème, and M. L. Goldstein (2016), Transport of solar wind H+ and He++ ions across Earth's bow shock, *The Astrophysical Journal*, *825*(2), L27, doi:10.3847/2041-8205/825/2/L27.

Persson, M., Y. Futaana, A. Fedorov, H. Nilsson, M. Hamrin, and S. Barabash (2018), H^+/O^+ Escape Rate Ratio in the Venus Magnetotail and its Dependence on the Solar Cycle, *Geophysical Research Letters*, *45*(20), 10,805–10,811, doi:10.1029/2018GL079454.

Russell, C., S. Mayerberger, and X. Blanco-Cano (2006a), Proton cyclotron waves at Mars and Venus, *Advances in Space Research*, *38*(4), 745–751, doi:10.1016/j.asr.2005.02.091.

Russell, C., J. Luhmann, and R. Strangeway (2006b), The solar wind interaction with Venus through the eyes of the Pioneer Venus Orbiter, *Planetary and Space Science*, *54*(13-14), 1482–1495, doi:10.1016/j.pss.2006.04.025.

Russell, C. T., J. G. Luhmann, K. Schwingenschuh, W. Riedler, and Y. Yeroshenko (1990), Upstream waves at Mars: Phobos observations, *Geophysical Research Letters*, *17*(6), 897–900, doi:10.1029/GL017i006p00897.

Russell, C. T., T. L. Zhang, M. Delva, W. Magnes, R. J. Strangeway, and H. Y. Wei (2007), Lightning on Venus inferred from whistler-mode waves in the ionosphere, *Nature*, *450*(7170), 661–662, doi:10.1038/nature05930.

Scarf, F. L., W. W. L. Taylor, C. T. Russell, and L. H. Brace (1980a), Lightning on Venus: Orbiter detection of whistler signals, *Journal of Geophysical Research*, *85*(A13), 8158, doi:10.1029/JA085iA13p08158.

Scarf, F. L., W. W. L. Taylor, C. T. Russell, and R. C. Elphic (1980b), Pioneer Venus plasma wave observations: The solar wind-Venus interaction, *Journal of Geophysical Research*, *85*(A13), 7599, doi:10.1029/JA085iA13p07599.

Sckopke, N., G. Paschmann, A. L. Brinca, C. W. Carlson, and H. Lühr (1990), Ion thermalization in quasi-perpendicular shocks involving reflected ions, *Journal of Geophysical Research*, *95*(A5), 6337, doi:10.1029/JA095iA05p06337.

Song, P., C. T. Russell, and S. P. Gary (1994), Identification of low-frequency fluctuations in the terrestrial magnetosheath, *Journal of Geophysical Research*, *99*(A4), 6011–6025, doi:10.1029/93JA03300.

Sperveslage, K., F. M. Neubauer, K. Baumgärtel, and N. F. Ness (2000), Magnetic holes in the solar wind between 0.3 AU and 17 AU, *Nonlinear Processes in Geophysics*, *7*, 191–200, doi:10.5194/npg-7-191-2000.

Stenberg Wieser, G., M. Ashfaque, H. Nilsson, Y. Futaana, S. Barabash, C. Diéval, A. Fedorov, and T. Zhang (2015), Proton and alpha particle precipitation onto the upper atmosphere of Venus, *Planetary and Space Science*, *113-114*, 369–377, doi:10.1016/j.pss.2015.01.018.

Svedhem, H., D. Titov, D. McCoy, J.-P. Lebreton, S. Barabash, J.-L. Bertaux, P. Drossart, V. Formisano, B. Häusler, O. Korablev, W. Markiewicz, D. Nevejans, M. Pätzold, G. Piccioni, T. Zhang, F. Taylor, E. Lellouch, D. Koschny, O. Witasse, H. Eggel, M. Warhaut, A. Accomazzo, J. Rodriguez-Canabal, J. Fabrega, T. Schirmann, A. Clochet, and M. Coradini (2007), Venus Express—The first European mission to Venus, *Planetary and Space Science*, *55*(12), 1636–1652, doi:10.1016/j.pss.2007.01.013.

Titov, D., H. Svedhem, D. Koschny, R. Hoofs, S. Barabash, J.-L. Bertaux, P. Drossart, V. Formisano, B. Häusler, O. Korablev, W. Markiewicz, D. Nevejans, M. Pätzold, G. Piccioni, T. Zhang, D. Merritt, O. Witasse, J. Zender, A. Accomazzo, M. Sweeney, D. Trillard, M. Janvier, and A. Clochet (2006), Venus Express science planning, *Planetary and Space Science*, *54*(13-14), 1279–1297, doi:10.1016/j.pss.2006.04.017.

Tsurutani, B. T., and E. J. Smith (1986), Hydromagnetic waves and instabilities associated with cometary ion pickup: ICE observations, *Geophysical Research Letters*, *13*(3), 263–266, doi:10.1029/GL013i003p00263.

Volwerk, M., T. L. Zhang, M. Delva, Z. Vörös, W. Baumjohann, and K.-H. Glassmeier (2008a), First identification of mirror mode waves in Venus' magnetosheath?, *Geophysical Research Letters*, *35*(L12204), doi:10.1029/2008GL033621.

Volwerk, M., T. L. Zhang, M. Delva, Z. Vörös, W. Baumjohann, and K.-H. Glassmeier (2008b), Mirror-mode-like structures in Venus' induced magnetosphere, *Journal of Geophysical Research*, *113*(E00B16), doi:10.1029/2008JE003154.

Volwerk, M., D. Schmid, B. T. Tsurutani, M. Delva, F. Plaschke, Y. Narita, T. Zhang, and K.-H. Glassmeier (2016), Mirror mode waves in Venus's magnetosheath: solar minimum vs. solar maximum, *Annales Geophysicae*, *34*(11), 1099–1108, doi:10.5194/angeo-34-1099-2016.

Waara, M., R. Slapak, H. Nilsson, G. Stenberg, M. André, and I. A. Barghouthi (2011), Statistical evidence for O+ energization and outflow caused by wave-particle interaction in the high altitude cusp and mantle, *Annales Geophysicae*, *29*(5), 945–954, doi:10.5194/angeo-29-945-2011.

Wei, H., C. Russell, T. Zhang, and X. Blanco-Cano (2011), Comparative study of ion cyclotron waves at Mars, Venus and Earth, *Planetary and Space Science*, *59*(10), 1039–1047, doi:10.1016/j.pss.2010.01.004.

Whittaker, I., G. Guymer, M. Grande, B. Pintér, S. Barabash, A. Federov, C. Mazelle, J. A. Sauvaud, R. Lundin, C. T. Russell, Y. Futaana, M. Fränz, T. L. Zhang, H. Andersson, A. Grigoriev, M. Holmström, M. Yamauchi, K. Asamura, W. Baumjohann, H. Lammer, A. J. Coates, D. O. Kataria, D. R. Linder, C. C. Curtis, K. C. Hsieh, H. E. J. Koskinen, E. Kallio, P. Riihelä, W. Schmidt, J. Kozyra, S. McKenna-Lawlor, J. J. Thocaven, S. Orsini, R. Cerulli-Irelli, A. Mura, M. Milillo, M. Maggi, E. Roelof, P. Brandt, R. A. Frahm, J. R. Sharber, P. Wurz, and P. Bochsler (2010), Venusian bow shock as seen by the ASPERA-4 ion instrument on Venus Express, *Journal of Geophysical Research: Space Physics*, *115*(A09224), doi:10.1029/2009JA014826.

Wilson III, L. B., M. L. Stevens, J. C. Kasper, K. G. Klein, B. A. Maruca, S. D. Bale, T. A. Bowen, M. P. Pulupa, and C. S. Salem (2018), The Statistical Properties of Solar Wind Temperature Parameters Near 1 au, *The Astrophysical Journal Supplement Series*, *236*(2), 41, doi:10.3847/1538-4365/aab71c.

Zhang, T., W. Baumjohann, M. Delva, H.-U. Auster, A. Balogh, C. Russell, S. Barabash, M. Balikhin, G. Berghofer, H. Biernat, H. Lammer, H. Lichtenegger, W. Magnes, R. Nakamura, T. Penz, K. Schwingenschuh, Z. Vörös, W. Zambelli, K.-H. Fornacon, K.-H. Glassmeier, I. Richter, C. Carr, K. Kudela, J. Shi, H. Zhao, U. Motschmann, and J.-P. Lebreton (2006), Magnetic field investigation of the Venus plasma environment: Expected new results from Venus Express, *Planetary and Space Science*, *54*(13-14), 1336–1343, doi:10.1016/j.pss.2006.04.018.

Zhang, T. L., J. G. Luhmann, and C. T. Russell (1991), The magnetic barrier at Venus, *Journal of Geophysical Research*, *96*(A7), 11,145, doi:10.1029/91JA00088.

Zhang, T. L., M. Delva, W. Baumjohann, M. Volwerk, C. T. Russell, H. Y. Wei, C. Wang, M. Balikhin, S. Barabash, H.-U. Auster, and K. Kudela (2008a), Induced magnetosphere and its outer boundary at Venus, *Journal of Geophysical Research*, *113*, doi:10.1029/2008JE003215.

Zhang, T. L., C. T. Russell, W. Baumjohann, L. K. Jian, M. A. Balikhin, J. B. Cao, C. Wang, X. Blanco-Cano, K.-H. Glassmeier, W. Zambelli, M. Volwerk, M. Delva, and Z. Vörös (2008b), Characteristic size and shape of the mirror mode structures in the solar wind at 0.72 AU, *Geophysical Research Letters*, *35*(L10106), doi:10.1029/2008GL033793.

Zhang, T. L., Q. M. Lu, W. Baumjohann, C. T. Russell, A. Fedorov, S. Barabash, A. J. Coates, A. M. Du, J. B. Cao, R. Nakamura, W. L. Teh, R. S. Wang, X. K. Dou, S. Wang, K. H. Glassmeier, H. U. Auster, and M. Balikhin (2012), Magnetic Reconnection in the Near Venusian Magnetotail, *Science*, *336*(6081), 567–570, doi:10.1126/science.1217013.

Figure 1.

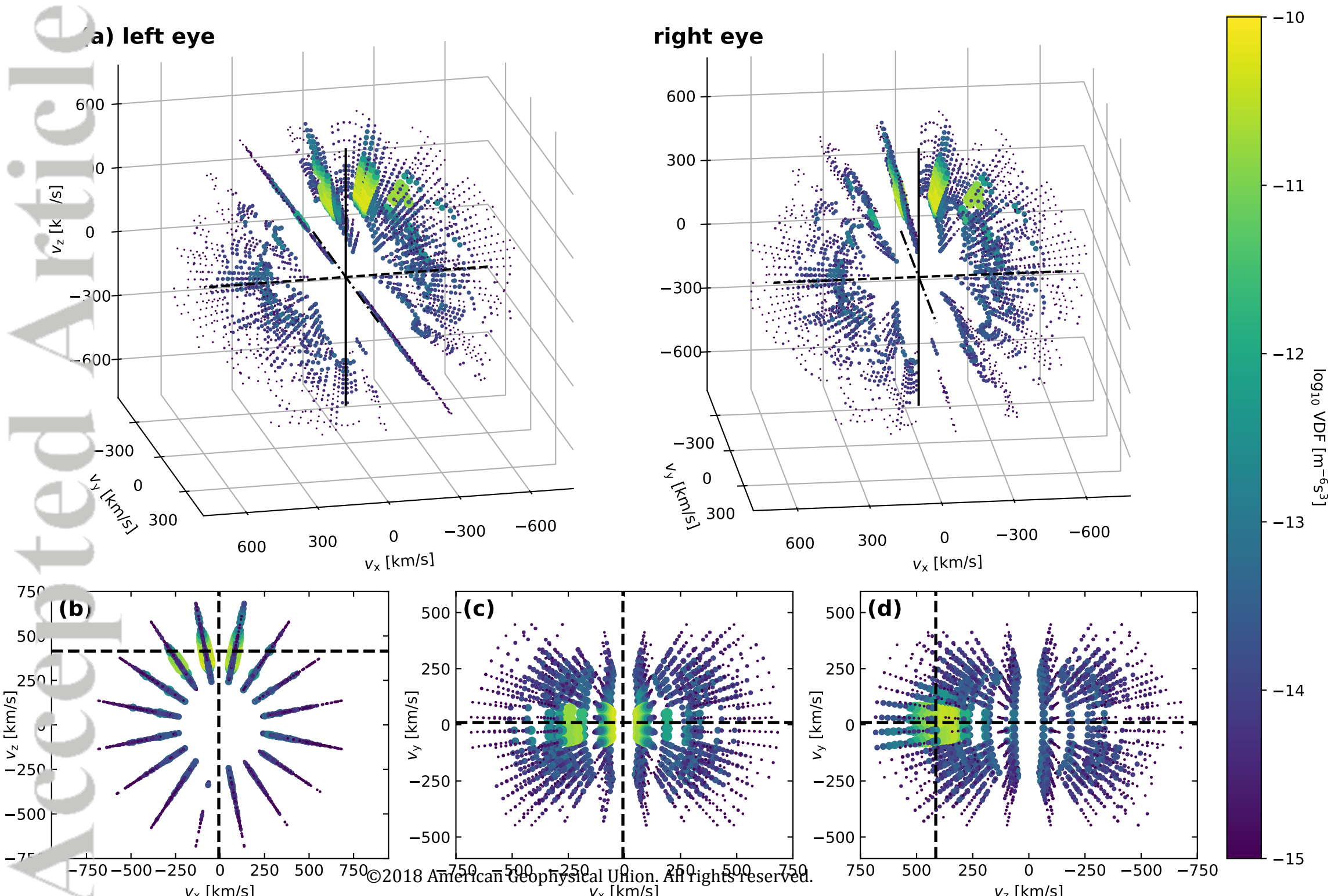

Figure 2.

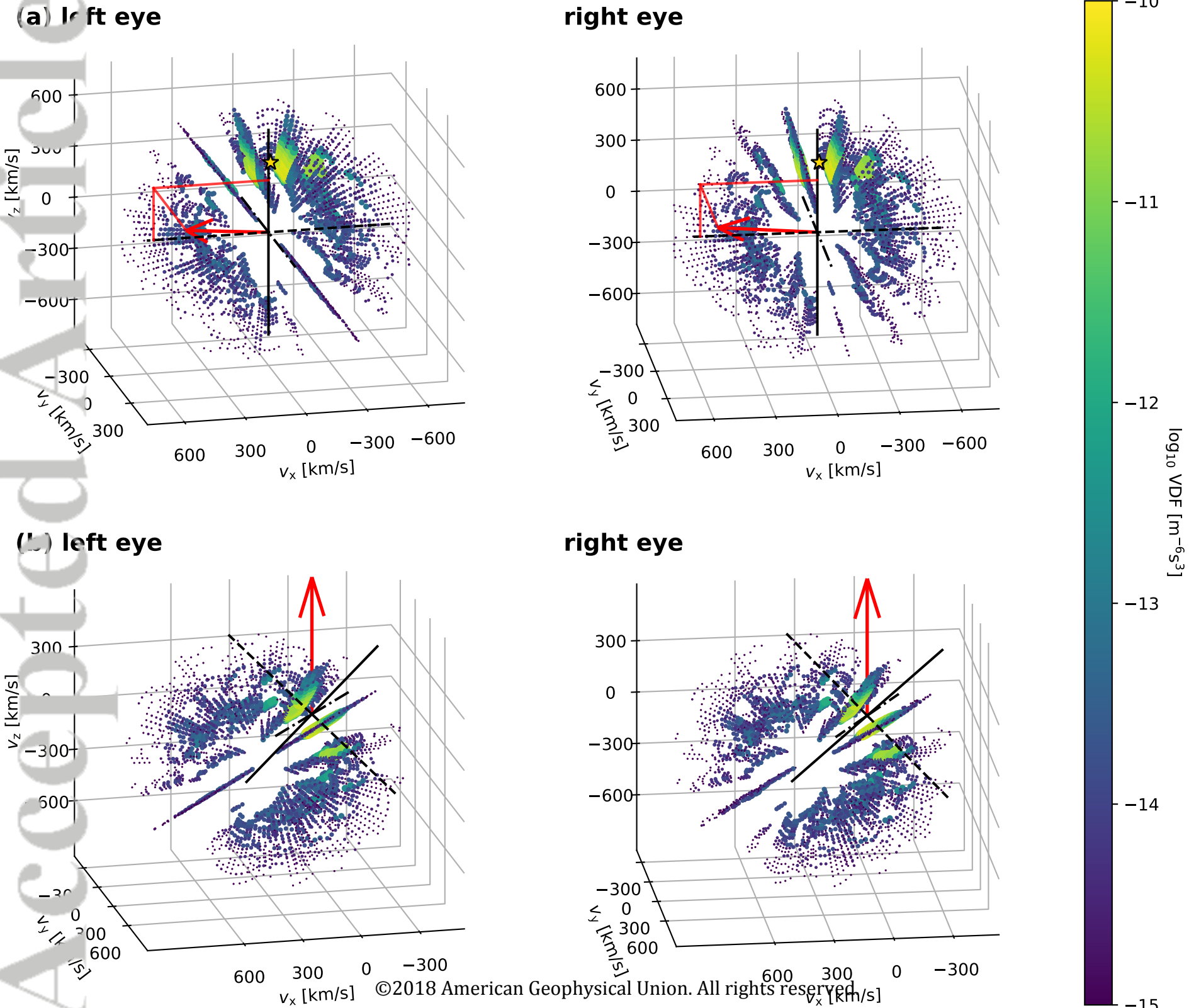

Figure 3.

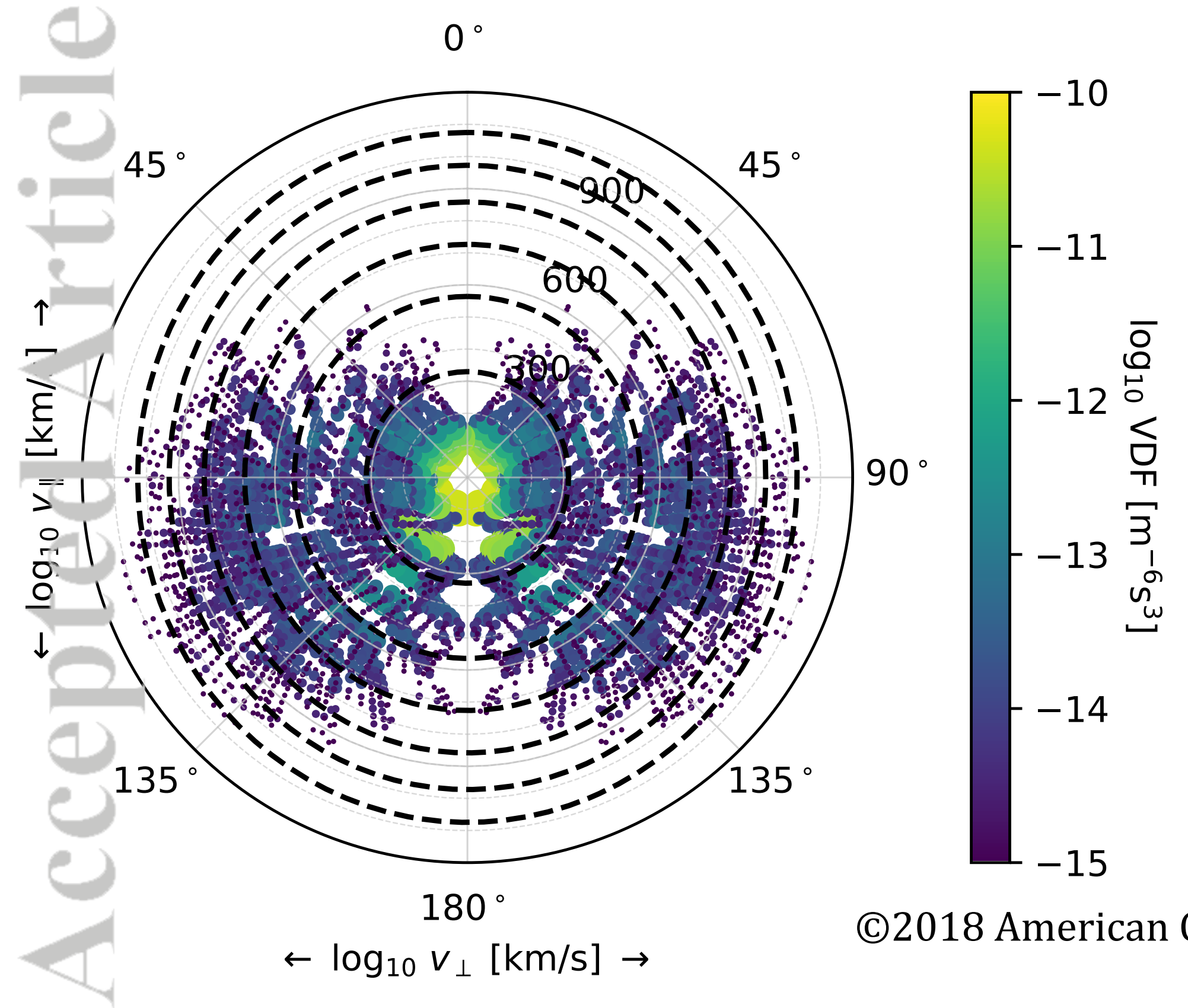

Figure 4.

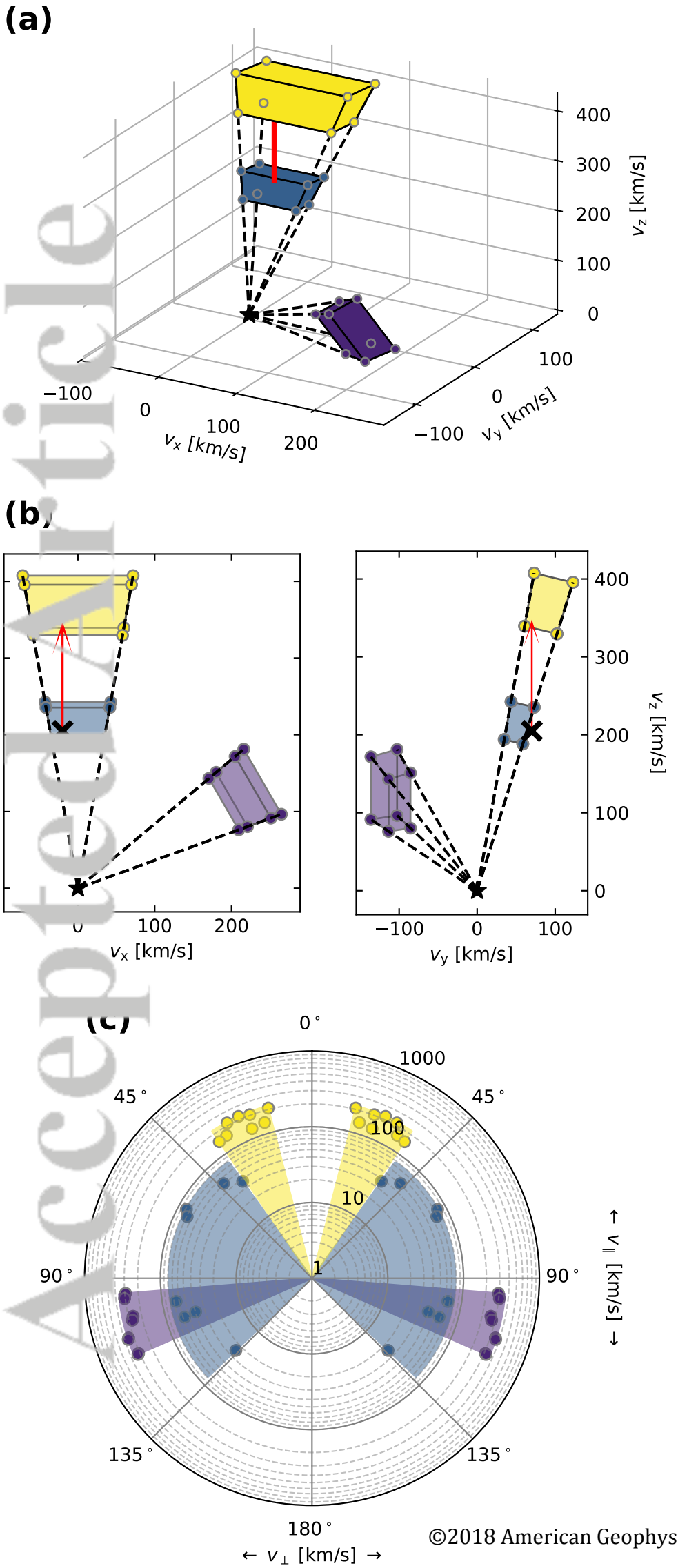

Figure 5.

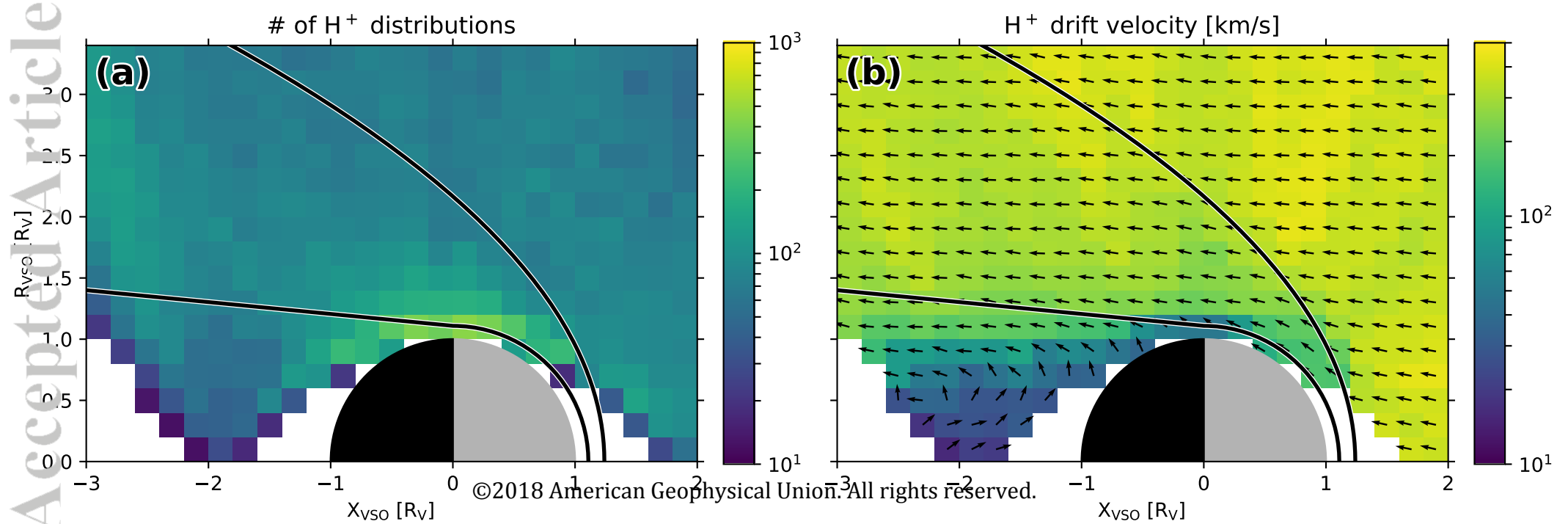

Figure 6.

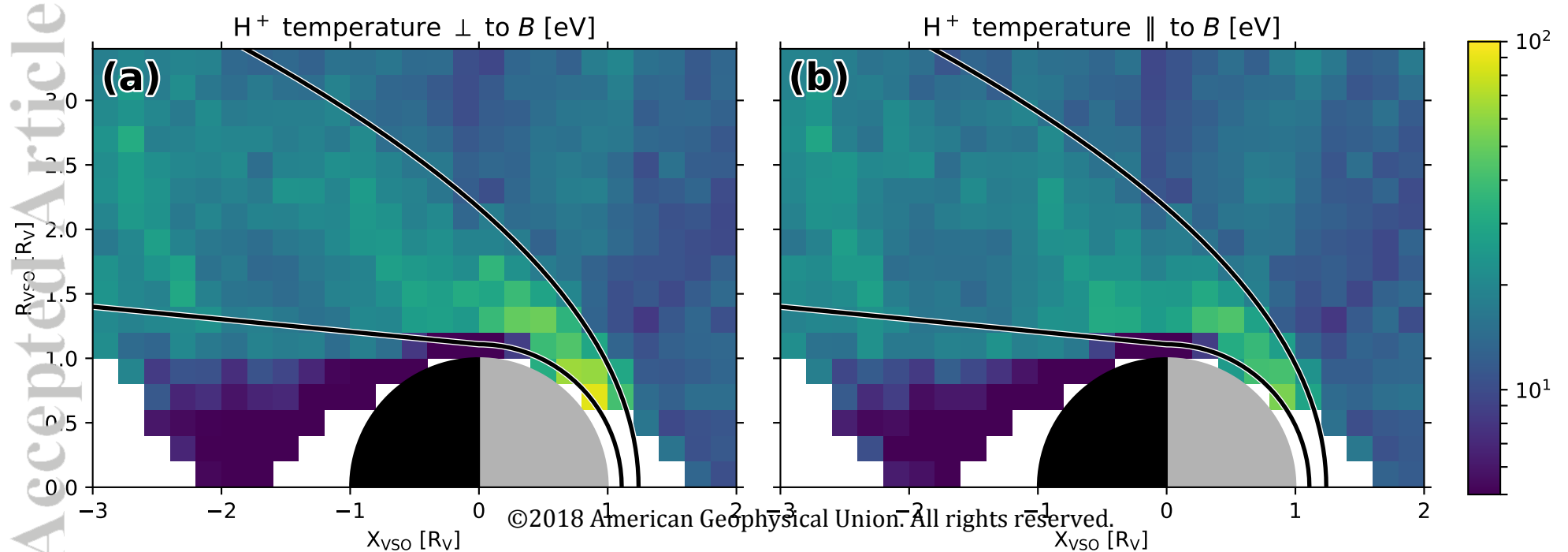

Figure 7.

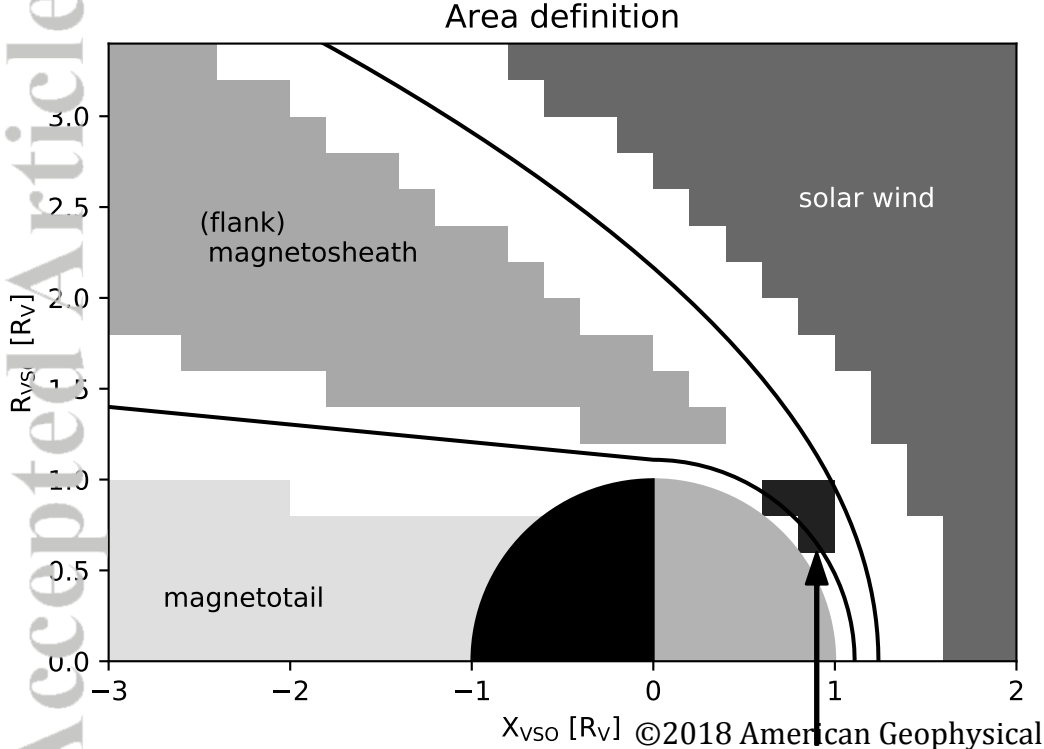

Figure 8.

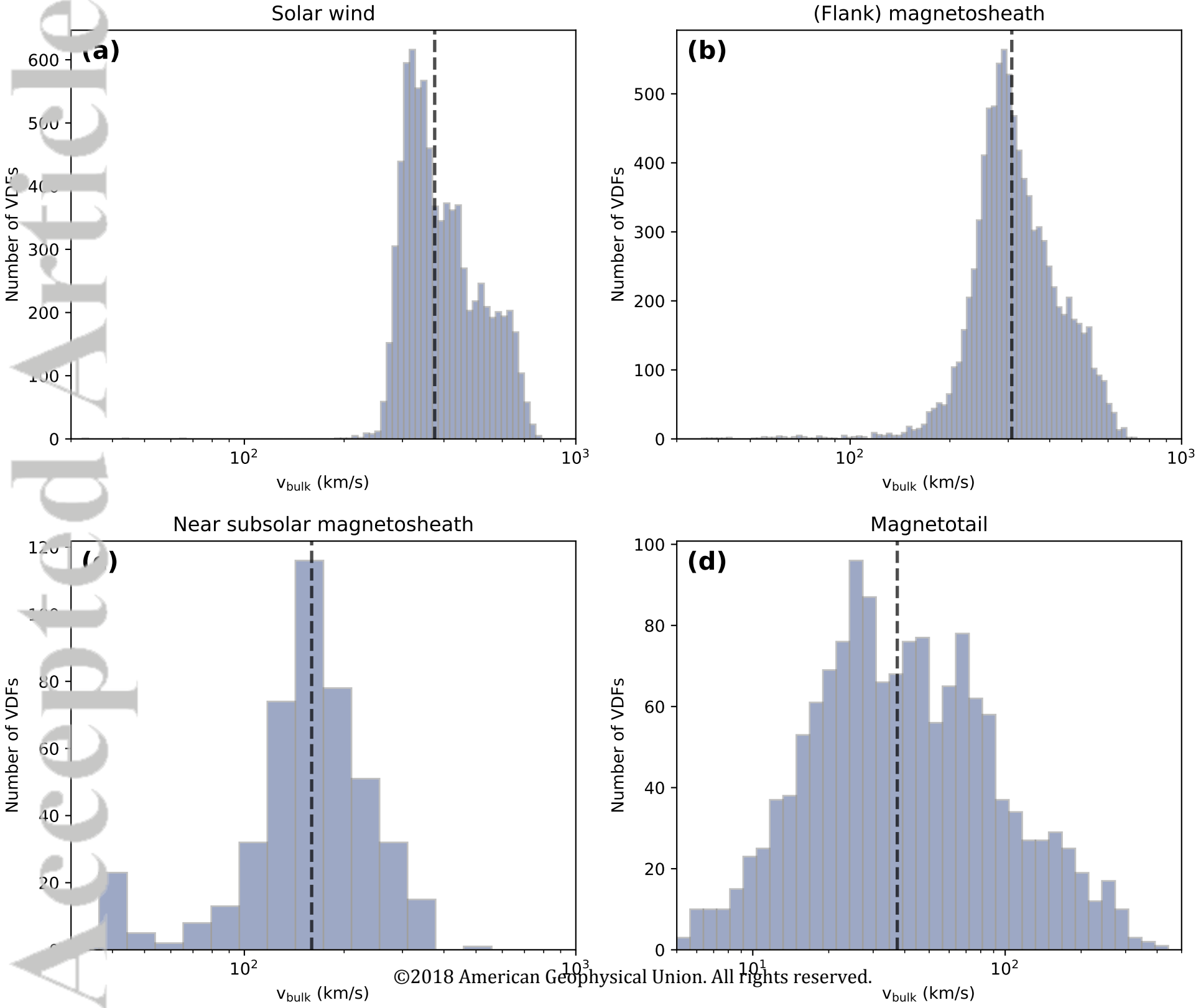

Figure 9.

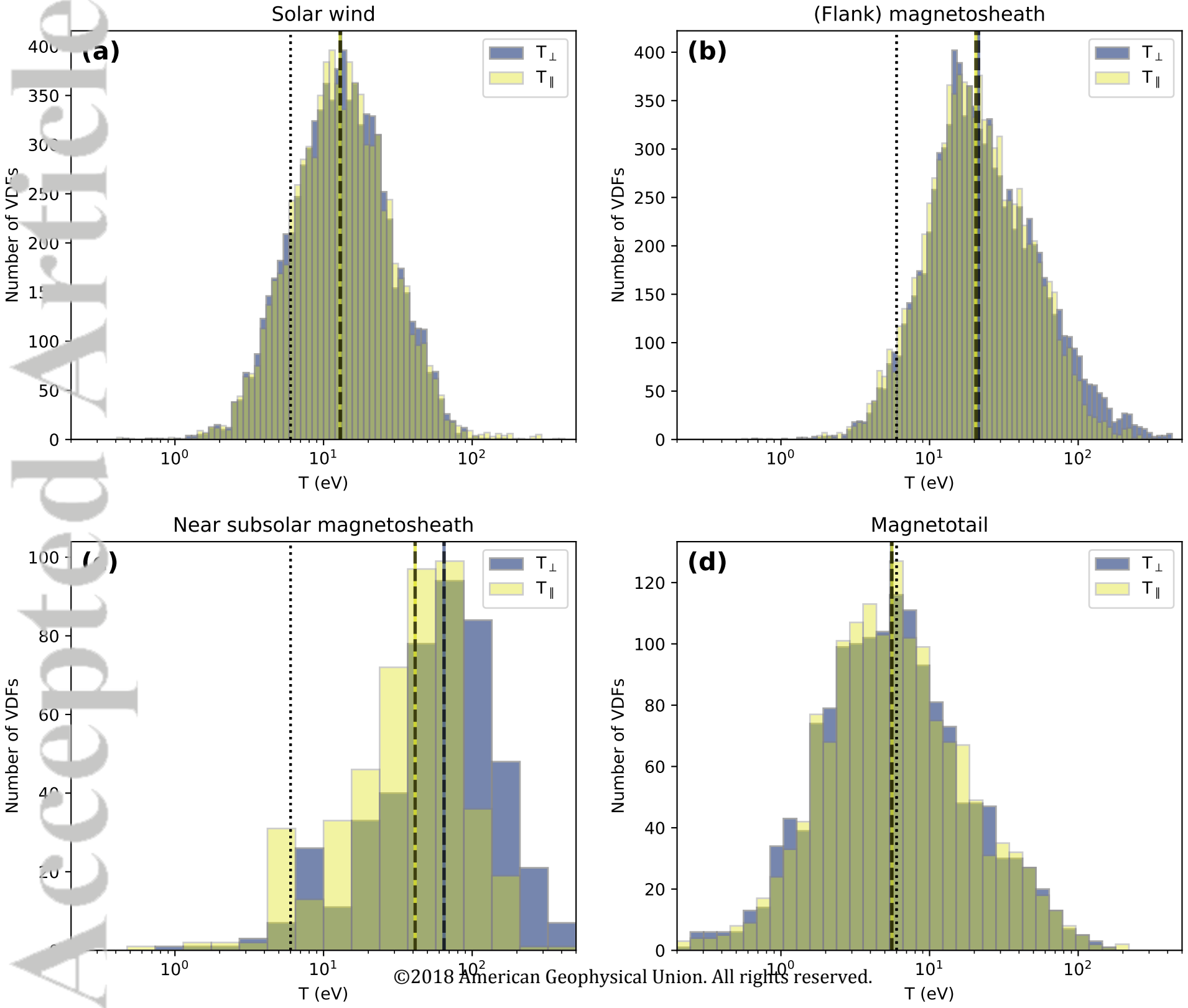

Figure 10.

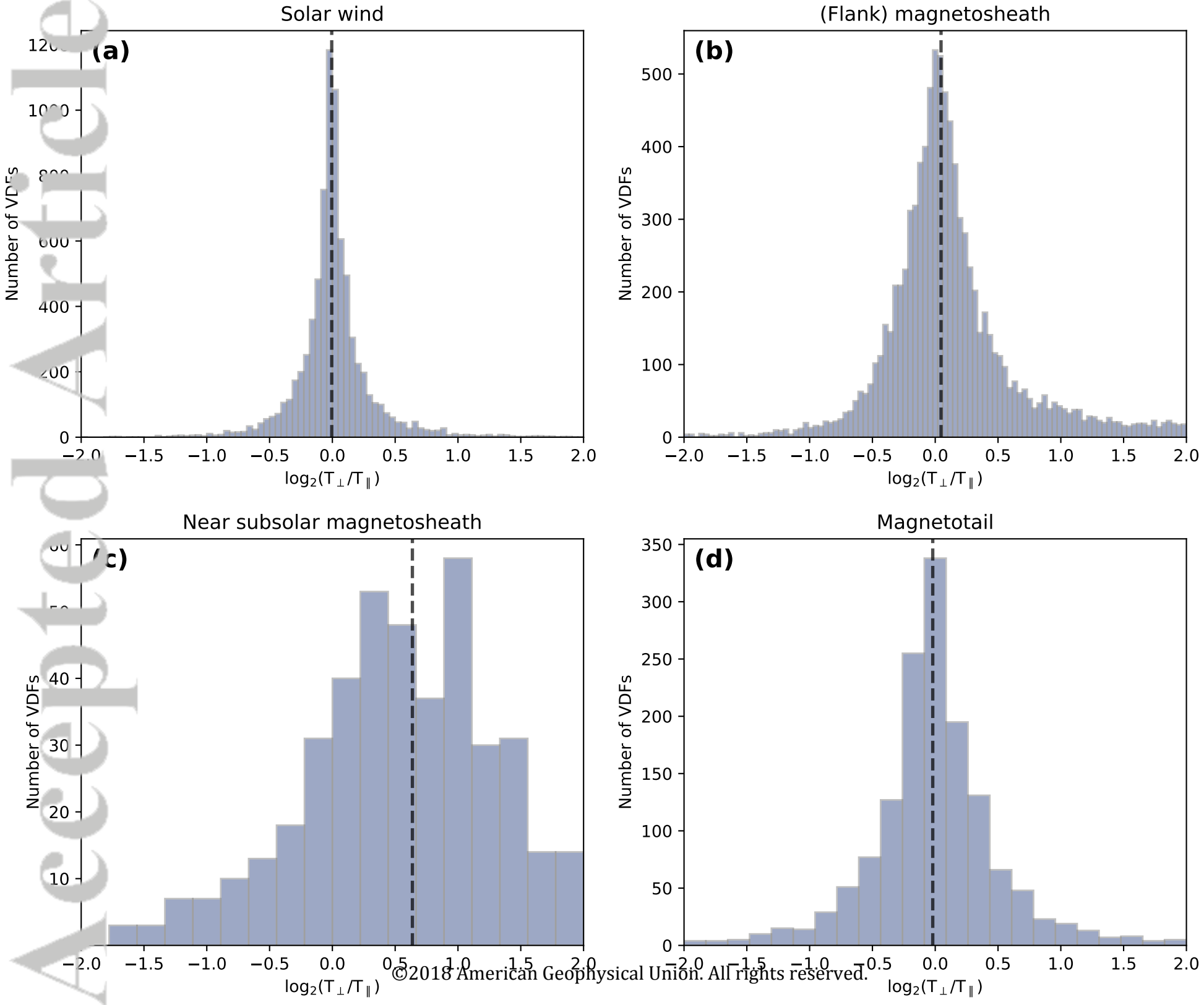

Figure 11.